Technische Universität München
TUM School of Engineering and Design

Melt Electrowriting:
Technological Advances and Cardiovascular Applications

Kilian Maria Arthur Müller

Vollständiger Abdruck der von der TUM School of Engineering and Design der Technischen Universität München zur Erlangung eines

Doktors der Ingenieurwissenschaften (Dr.-Ing.)

genehmigten Dissertation.

Vorsitz: Prof. Dr. Sonja Berensmeier

Prüfende der Dissertation:

1. Prof. Dr. Petra Mela
2. Assoc. Prof. Antonio D'Amore, Ph.D.
3. Assoc. Prof. Francesco Moscato, Ph.D.

Die Dissertation wurde am 02.10.2024 bei der Technischen Universität München eingereicht und durch die TUM School of Engineering and Design am 02.12.2024 angenommen.

Table of Contents

1. Summary

Melt electrowriting (MEW) is an electrohydrodynamic additive manufacturing technology for thermoplastic polymers enabling the fabrication of accurately organized microfiber architectures. This thesis contributes to the advancement of MEW by presenting innovations from three perspectives, specifically i) hardware components, ii) software tools, and iii) enhanced material functionality in the context of cardiovascular tissue engineering.

As alternative to conventional syringe-based print heads for MEW, a filament-based print head is presented. This concept transforms a fused filament fabrication (FFF) system into a MEW system with only minimal modifications required. The system is validated by melt electrowriting the gold standard polymer polycaprolactone, while the melt-on-demand concept of the print head additionally enables the processing of the thermosensitive polydioxanone via MEW. By using both the MEW mode and the FFF mode of the system, multi-scale additive manufacturing using the same print head is demonstrated. Furthermore, this machine design concept is making MEW accessible to the large FFF user community.

Next, an open-source 5-axis kinematic system is upgraded to implement the electric field components required for MEW. This, alongside a novel print head design with increased clearance, enables MEW onto complex multicurvature collectors with a freedom of design unconceivable with current MEW technology. Furthermore, a workflow to produce arbitrarily shaped collectors is proposed. This technology contribution is complemented by a universal graphical approach to generate toolpath commands for such complex print jobs. The potential of this system is demonstrated by fabricating reinforcement patterns for tissue-engineered trileaflet heart valves and bifurcating vessel grafts onto anatomically relevant collector geometries.

Besides technological advances, in this thesis new design strategies are developed that enable the fabrication of cardiovascular devices with advanced functionalities. In contrast to the inherent macroporosity of MEW constructs, tailored microporous scaffolds for tissue engineering are realized by superimposing angularly shifted arrays of parallel fiber sets. This concept avoids the negative effects of fiber bridging, decouples fiber diameter from pore size, and is applicable to both flat and tubular architectures. In addition, tunable mechanical anisotropy can be introduced to the scaffold architecture. Effective infiltration of the scaffolds by human umbilical artery smooth muscle cells is demonstrated.

Building on the microporous design strategy, the fiber winding angle of tubular architectures is systematically investigated to fabricate scaffolds for small-diameter vascular grafts with a tunable compliance. This aims at avoiding a compliance mismatch between native vessel and graft, which has been identified as a major contributor to long term graft failure. By adjusting the fiber winding angle, a tunable structure-function relationship is achieved, allowing for compliance values that span the range of native arteries and veins. Leveraging this knowledge, a gradient fiber architecture is realized to create a smooth transition between two distinct terminal compliances for arteriovenous grafts, addressing the difference between arterial and venous compliance at the anastomoses. The potential for clinical application of this new graft concept is further highlighted by meeting key requirements, including suture retention, resistance to kinking, burst pressure, and self-sealing after cannulation.

Lastly, to address the translational potential of melt-electrowritten implants, ultrasmall superparamagnetic iron oxide (USPIO) nanoparticles are incorporated into polycaprolactone to serve as contrast agent that increases imaging quality in magnetic resonance imaging (MRI). The composite materials are detected using T2- and T2*-weighted MRI, while cytocompatibility and mechanical properties remain adequate for tissue engineering applications.

2. General Introduction and Thesis Outline

Additive manufacturing (AM) has revolutionized the way mankind is producing objects across all scales. Among the variety of AM technologies,[1,2] extrusion-based approaches are the most accessible ones for processing thermoplastic polymers[3] with fused filament fabrication (FFF) having an exceptionally large user community that is continuously driving technological advancements.[4] However, FFF is limited to a resolution of about 100 µm in feature size.[3] This is due to i) the available nozzle sizes and ii) the die swelling phenomenon, where a non-Newtonian polymer melt expands to a diameter larger than that of the nozzle opening through which it is extruded.[5] Leveraging the effect of an electric field on the polymer, melt electrowriting (MEW) overcomes this resolution limitation by forming fibers significantly smaller than the nozzle orifice, hence, enabling the fabrication of objects from micron-sized fibers.

2.1. Process Principle of Melt Electrowriting

Over a decade ago, MEW was conceptualized as electrohydrodynamic process combining characteristics of extrusion-based AM with a high voltage electric field (**Figure 1**).[6] To this end, a thermoplastic polymer is melted and extruded through a nozzle as a pendant drop, which transforms into a Taylor cone under the influence of the electric field created between the nozzle and a collector.[7] This is due to the electric charges introduced into the polymer drop and the resulting repulsive forces that overcome its surface tension.[8] The Taylore cone further elongates generating a fiber jet that travels towards the electrically grounded or oppositely charged collector.[9] The charges prevent this fluid column (i.e. fiber jet) from breaking up due to Plateau-Rayleigh instabilities even at low flow rates (~ µL h^{-1}),[7,10] while its diameter asymptotically decays.[11] Collecting the fiber jet at a speed matching its travel speed on a collector moving according to a predefined path, results in controlled fiber deposition in a direct writing mode.[6] As the deposited fiber cools down, it solidifies on the collector so that a layered construct can be built by repeatedly stacking individual fibers on top of each other.[12]

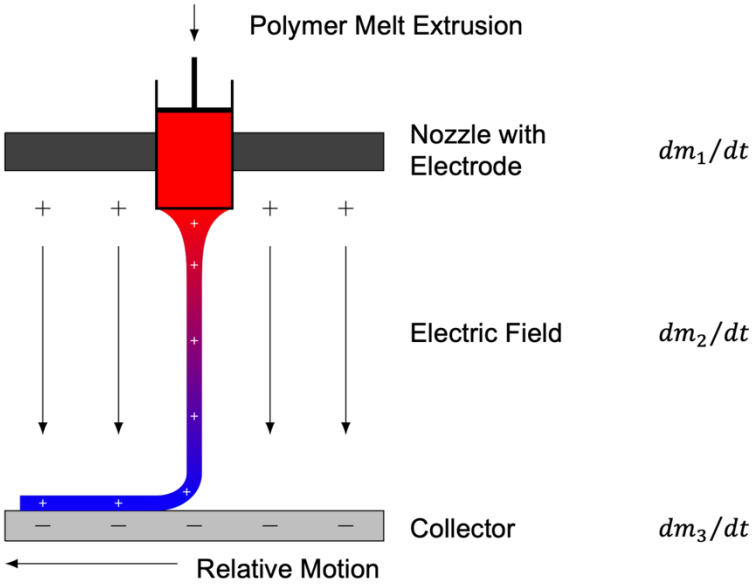

Figure 1: Schematic of the MEW process. A polymer melt is extruded through a nozzle (dm_1/dt). An electric field applied between the nozzle and the collector, separated by an air gap, transforms the polymer melt at the nozzle tip into a Taylor cone from which a fiber jet emerges that travels towards the collector (dm_2/dt). The electric forces stabilize the fiber jet during its flight phase while its diameter decays. Matching the collector's speed with the travel speed of the fiber jet allows for controlled deposition of the polymer fiber in a direct writing mode (dm_3/dt). As the polymer melt (indicated in red) cools down during the flight phase and solidifies (indicated in blue) onto the collector, the next fiber can be stacked onto the previously deposited one to form a layered construct.

MEW is a process of multi-parametric nature.[13] Its dynamically interrelated process parameters[14] can be differentiated into those that i) control the polymer mass flow through the nozzle (dm_1/dt), ii) regulate the mass flow of the fiber jet in the flight phase (dm_2/dt), and iii) set the mass flow when depositing the fiber onto the collector (dm_3/dt) (**Figure 1**).[15] Also environmental conditions such as ambient temperature and humidity need to be considered.[14] Stable process conditions are a *conditio sine qua non* for reproducible fabrication, and are only obtained if the three mass flows are in balance.[15] The most important parameters influencing dm_1/dt are melt viscosity, melt temperature, and melt feed rate[14,16] and dm_2/dt is predominantly controlled via the electric field parameters, while the environmental conditions affect how many charges are depleted into the ambient atmosphere.[17]

If dm_1/dt is not in balance with dm_2/dt, time-variant fiber diameters result. This manifests in fiber pulsing (high frequency oscillations in fiber diameter)[18] or long beading (occasional large fiber diameter outliers)[15] and can be remedied by increasing the applied voltage and/or decreasing the melt feed rate in case $dm_1/dt > dm_2/dt$.[14] Switching the polarity of the electric field does not affect fiber diameter stability,[19,20] while contradictory effects on jet speed were reported.[19,20] Specifically, Hrynevich found faster jets when a positive polarity was applied to the needle,[19] while Lu *et al.* did not observe differences in jet speed after switching the polarity.[20]

Matching the collector speed to that of the fiber jet enables accurate fiber deposition along the collector's toolpaths. This speed is termed the critical translation speed (CTS).[6] At slower collector speeds the fiber jet undergoes buckling due to axial compression when impacting the collector, resulting in coiled fiber deposition (e.g. chaotic whipping, figures of eight, undulations).[6,21] Higher collector speeds introduce a pulling force to the jet, giving rise to its characteristic curved profile,[6] which can be described by a catenary curvature.[22] This, however, causes a jet lag which shifts the jet's collector contact point with respect to the projected nozzle position, hence, reducing pattern fidelity.[23,24] Algorithmically derived and correspondingly oversized toolpaths can help compensating for this spatial offset.[23,25] The majority of MEW research is performed at speeds slightly above CTS (~ 110 % CTS), to introduce a safety margin in order to avoid jet buckling. Excessively high collector speeds (> 3 x CTS) result in a pulling effect on the jet that further increases the jet lag and reduces fiber diameter.[26]

A stabilization of the jet has to be performed prior to the printing process to achieve satisfactory results and the same conditions need to be maintained throughout the whole process.[26] This results in the fact that the fiber jet cannot be stopped and restarted as typically done in FFF. Therefore, in MEW the toolpaths must be continuous.

Finding optimized parameter sets is still mostly based on the operators' experience. Yet, there is more than a decade of knowledge from multiple laboratory groups to build on.[14] Furthermore, first attempts of using machine vision for in-line process control[27] and machine learning for informed suggestions of parameter sets[28] have been made.

2.2. Technology for Melt Electrowriting

A MEW system requires five key components for operation: i) a polymer melt extrusion system (i.e. print head), ii) a collector, iii) a kinematic system for the relative movement of print head and collector, iv) toolpath commands to control the kinematic system, and v) a high voltage source to establish an electric field between the extrusion system and the collector.

Print Head

MEW print heads were first designed following a syringe-based approach, where granulates of a feedstock polymer are contained in a syringe, thermally liquefied, and extruded via a programmable syringe pump.[6] To date pressurized gas, primarily air, applied to the syringe has replaced the syringe pump in most MEW print heads.[29–35] In early systems, the syringe was placed inside a water jacket housing through which

temperature controlled water was circulating.[6] Advanced systems build on resistive heating to control the melt temperature, often with two different zones (syringe and nozzle),[29–35] while a minority of systems use heat guns.[17,36,37] The employed syringes are either from plastic or glass and equipped with a Luer lock fitting to mount a metallic needle, with an orifice typically in the range of 30 G to 21 G (0.159 mm to 0.514 mm).[38] Using a coaxial needle, enables the fabrication of hollow fibers.[39] The needle is in contact with an electrode to which one polarity of the high voltage is applied. Flat electrodes, from which the needle protrudes about 1 mm are the gold standard.[40] Due to the proximity of the heating systems and the high voltage components careful design of the print head is required to avoid arcing into sensitive components. Recent studies have explored the potential for upscaling fiber production by equipping MEW systems with multiple print heads in parallel[29] or by providing a single print head with a pair of parallel nozzles.[41]

Collector

MEW inherently requires a collector, to which one terminal of the high voltage power supply is connected, to deposit the fiber jet onto. The collector geometry, therefore, defines the resulting scaffold's 3D shape. MEW was first presented onto a flat collector resulting in sheet-like constructs.[6] Soon after, prints were performed onto a cylindrical collector to fabricate tubular structures.[42] To date, tubular scaffolds with inner diameters ranging from 0.5 mm[43] to 22 mm[44] were manufactured.

The collector surface ideally is of a conductive material, otherwise the electric charges entrapped in the deposited fibers would accumulate, leading to fiber repulsion, which in turn prevents fiber stacking.[17] MEW onto thin glass microscope slides placed directly on top of the collector surface is commonly done, to enable fast optical characterization after printing.[45]

Similar to heated print beds in FFF, flat collectors are usually equipped with a heating system, to control the cool-down phase of the deposited polymer.[29–35,46] If at all, tubular collectors are so far only indirectly heated via heated components in their vicinity that are e.g. mounted on the underlying flat collector.[47]

To date, attempts to fabricate constructs beyond sheet-like or tubular geometries are limited to printing onto 3D molds (e.g. domes) placed on flat collectors[48–51] or tubular collectors with changing diameters using 3-axis kinematic systems.[52,53]

Kinematic System

The kinematic system executes the relative motion between print head and collector. This crucial component enables direct writing of the fiber jet onto the collector along computer-controlled toolpaths. Various concepts for kinematic systems in MEW exist.

MEW was first presented with an orthogonal assembly of two stages in X-Y configuration to position a planar collector.[6] Adding a Z-axis allowed to set the working distance (gap between print head and collector) in a computer-controlled manner. To enable MEW onto cylindrical collectors one of the translating X- or Y-axis is replaced with a rotational axis.[42]

Kinematic systems based on stepper motor-driven lead screw stages[24,29–33,54–57] or in combination with belt/pulley configurations[35,47,48,58] were in-house developed for MEW. Such systems can even include closed-loop positioning to eliminate step losses.[31] Other kinematic systems were integrated as complete solutions from commercial providers.[59–61] With the aim of increasing accessibility, researchers have also proposed to exploit existing kinematic systems for MEW such as those from FFF[35,48] or from an automated dispensing system.[34] A 6-axis robotic arm has recently been used to perform MEW onto a spherical collector.[62] However, direct writing of the fiber jet failed, as relative speeds consistently above the CTS could not be achieved.

Toolpath Generator

The kinematic systems are mostly controlled via a series of Gcode commands which encode the toolpaths. Gcode stands for geometric code and is a programming language for CNC (Computer Numerical Control) machines. Linear movements are described via G1 followed by the coordinates of the target point. Circular movements are controlled via G2 (clockwise rotation) and G3 (anticlockwise rotation) commands. These do not only require the coordinates of the target point, but also coordinates for the center point of rotation. Alternatively, a G2 or G3 command can be replaced by a series of G1 commands that interpolate the non-linear movement via multiple small linear segments. Gcode can be programmed either in absolute (G90) or relative (G91) coordinates. Further Gcode commands exist to execute specific routines, such as axis homing (G28). The coordinates required for the individual Gcode commands can be derived via geometrical and trigonometrical considerations. In case of Gcodes for tubular constructs coordinate transformations have to be used to change from cartesian systems to polar systems and vice versa.

In agreement with the continuous fiber deposition of MEW, Gcodes are designed as non-interrupted toolpath following a line-based way of thinking. This is in strong contrast to

FFF, where a slicer software automatically converts a digital 3D model into toolpaths, which can also entail travel moves, where no material is extruded. As, to date, there is no universal slicer compatible with MEW, most Gcodes are manually composed.

Nevertheless, the design library of patterns for MEW fiber constructs advanced from cross hatch patterns[12] to highly tunable linear[59,63,64] and non-linear fiber arrangements[65], including wavy[66,67] and auxetic[68,69] architectures, both for flat and tubular constructs. To cope with the increasing design variability of patterns, specialized toolboxes, mostly based on MATLAB or Python, were developed to output complex patterns tailored to a specific use case.[25,44,59,63,70]

2.3. Melt Electrowriting in Context with Fiber-forming and Extrusion-based Technologies

MEW can be considered a hybrid technology arising from the combination of process characteristics of melt-electrospinning and melt-extrusion additive manufacturing, such as FFF. Electrospinning creates fibers with a diameter in the nano to micro range by applying a high voltage electric field to a constantly extruded polymer melt or solution.[71,72] However, as the fiber jet is collected under whipping conditions, fiber deposition is random and a non-woven fabric is formed, where fiber diameter and pore size correlate.[73,74] Fiber orientation can be influenced to a limited extent by using patterned collectors[75] or by collecting the fiber jet onto a rotating cylindrical mandrel to introduce structural anisotropy by aligning the fibers along the circumferential direction.[76]

In contrast, FFF produces fibers from a polymer melt by extrusion only.[5,77] Therefore, the resulting minimal feature size is determined by the size of the nozzle orifice, which is mostly larger than 150 µm and typically 400 µm in diameter.[78] An advantage of FFF is, however, its capability for controlled material deposition in three dimensions according to predefined pathways derived from a virtual 3D part model, hence qualifying as additive manufacturing technology.[78]

With respect to the fiber dimensions, MEW positions itself between electrospinning and FFF (**Figure 2**),[26] closing the fabrication gap between these technologies.

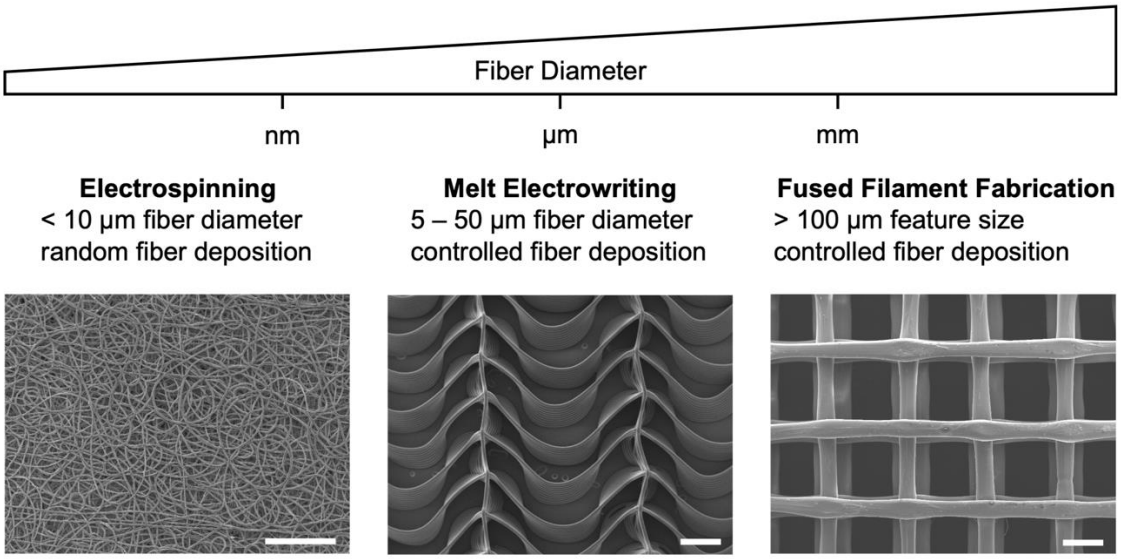

Figure 2: Melt electrowriting in context with other fiber-forming technologies. Electrospinning is capable of producing fibers in the nano to micro range from polymer melts or solutions, fiber deposition is random, hence dense non-woven textiles are formed (scale bar 100 µm). Melt electrowriting combines microfiber formation with controlled fiber deposition, thus, by repeatedly stacking fiber layers, complying with the paradigm of additive manufacturing (scale bar 500 µm). Fibers extruded via fused filament fabrication are usually larger than 100 µm in diameter and used to build objects according to virtual models in the cm scale or larger (scale bar 500 µm). Indicated fiber diameter ranges serve as orientation and are not to be understood as strict limitations.

2.4. Thesis Rational, Objectives, and Outline

Despite the promising conceptual fundament of MEW, its potential is still underexplored as challenges regarding the process technology remain, which result in strongly limited choice of materials and freedom of design.

The development of MEW technology has so far been driven by only few academic research groups, with a limited number of MEW machines being commercially available, which, though, do not offer the flexibility of the systems designed by academia.[12,14] This strongly limits the accessibility of MEW.[14] Driven by a large user community, the history of FFF technology development has impressively demonstrated the power of collaborative and open-source design approaches for advancing extrusion-based AM technology.[4,79] However, this potential has not yet been unlocked for MEW. Limitations of MEW can be found on the hardware, software, and application level, as outlined below.

Conventional MEW print heads are syringe-based.[29–35,38] As the mass flow required for microfiber fabrication is very low (~ µL h^{-1}),[7,10] this brings the consequence that the entire polymer feedstock contained in the syringe is exposed to melt temperature for an extended period of time, up to multiple weeks.[80] While this has been shown to be

unproblematic for polycaprolactone,[80] the most widely used polymer for MEW, the thermal stress is detrimental if not prohibitive to the processing of thermosensitive polymers.[81]

So far, melt-electrowritten architectures are limited to trivial shapes, being either sheet-like constructs or tubular designs. There have been only few reports of attempts to out-of-plane MEW, either performed on 3D molds placed on flat collectors[48–50,82] or by printing onto tubular collectors with varying diameters.[52,53] To date, MEW has not reached yet the freedom of design enabled by other AM technologies, hence the anatomical relevance of melt-electrowritten constructs is still limited.

Melt-electrowritten constructs have been widely used as scaffolds across various disciplines of tissue engineering (TE).[12,83] The recent paradigm shift from *in vitro* TE to *in situ* TE for cardiovascular applications calls for highly defined microporous scaffolds to allow for endogenous cell infiltration and tissue formation.[84] While MEW scaffolds have been utilized for their tunable structure-property relationship, they are typically macroporous and require the combination with another biomaterial and/or biofabrication process to obtain the desired microporosity.[44,85,86] Controlled microporosity is prohibited by the so-called fiber bridging effect, where fibers, if positioned closer to each other than a certain threshold distance, deviate from the planned deposition path due to electrostatic effects, bridge, and fuse together resulting in non-controlled patterns and, correspondingly, loss over control of mechanical properties.[87]

Cardiovascular TE sets the strict requirement that implants need to be functioning mechanically adequately upon implantation.[88] Compliance is a crucial mechanical property of small-diameter vascular grafts, that, if ignored, causes adverse biological responses, ultimately leading to graft failure.[89] While a variety of mechanical properties of MEW scaffolds has been specifically tailored to those of native cardiovascular tissues,[66,69,90,91] tuning the compliance based on MEW scaffold design parameters alone has not yet been systematically investigated.

Clinical translation of tissue-engineered implants demands the capability for longitudinal monitoring via a clinically accepted imaging technique, such as magnetic resonance imaging (MRI). While polymers are in general difficult to image via MRI due to their low proton density, the small volume of microfibrous MEW scaffolds additionally complicates this quest. Employing contrast agents to increase imaging quality in MRI is clinical routine,[92,93] however, this has not yet been successfully translated for MRI of melt-electrowritten constructs.

In light of these challenges, the overall aim of this thesis is to advance the MEW technology while simultaneously making it more accessible, to introduce new polymers with added functionality to the MEW material library, and to outline design strategies for the fabrication of anatomically relevant and mechanically adequate scaffolds for cardiovascular applications with a true potential for successful clinical translation. Specifically, the objectives of this thesis target the technological level (I.-IV.) and material functionality for cardiovascular applications (V.-VII.):

I. to **expand the MEW material library** by reducing the thermal load to the feedstock polymer

II. to **unlock freedom of design** for MEW scaffolds beyond flat or tubular geometries

III. to **increase the accessibility of MEW** technology

IV. to develop **a universal MEW Gcode generator**

V. to achieve **microporous scaffold architectures** by MEW only

VI. to enable **compliance by design** of MEW-based vascular graft scaffolds

VII. to allow for **monitoring of MEW scaffolds** via a clinically accepted imaging technique

Chapter 4 outlines the design of a syringe-based melt electrowriting platform for both flat and tubular melt electrowriting. The print head enables the use of plastic syringes (for melting temperatures up to 110 °C) or glass syringes (for melting temperatures up to 220 °C) while the flat collector assembly can be heated up to 150 °C and can optionally be expanded with an additional rotating axis to allow for tubular MEW.

Chapter 5 describes the development of a filament-based melt electrowriting system that builds on the technology ecosystem of FFF and leverages the melt-on-demand approach. The system is validated by processing polycaprolactone and thermosensitive polydioxanone is melt-electrowritten for the first time. Multi-scale AM is demonstrated with this system by exploiting both its MEW mode and its FFF mode in a single print job.

Chapter 6 outlines the design of a 5-axis kinematic system for MEW. Together with a novel print head design with increased clearance and a graphical approach to generate toolpath commands, this enables MEW onto collector geometries of a complexity

unconceivable with the currently available technology, thus realizing scaffolds with exceptional anatomical relevance.

Chapter 7 presents an overview of cardiovascular applications of melt-electrowritten constructs, specifically for capillary networks, cardiac patches, vascular grafts, and heart valves. Also, material and technological advancements are discussed in this context.

Chapter 8 introduces a design strategy to produce microporous constructs via MEW with pore sizes decoupled from the fiber diameter and without fiber bridging. Furthermore, tunable mechanical anisotropy and successful cell ingrowth into the constructs are demonstrated. Lastly, the potential of the design strategy for vascular grafts and covered stents is shown.

Chapter 9 builds on the design strategy presented in the previous chapter and advances this concept for the fabrication of small-diameter vascular grafts with tunable compliance. A compliance gradient from the proximal to the distal end of the graft is realized via a gradient fiber architecture.

Chapter 10 aims at facilitating clinical translation of melt-electrowritten constructs by enabling MRI of melt-electrowritten polycaprolactone scaffolds labeled with ultrasmall superparamagnetic iron oxide (USPIO) nanoparticles, which serve as contrast agent.

Chapter 11 concludes this thesis with a summary of the presented results and provides an outlook to potential future developments of MEW.

3. Materials and Methods

3.1. Materials

Biocompatible and biodegradable thermoplastic polymers are of particular interest in this thesis as cardiovascular tissue engineering applications of melt-electrowritten constructs are at its center. Thermoplastic polymers consist of macromolecules that interact via secondary intermolecular forces (e.g. hydrogen-bridges, van der Waals forces), which get weaker with increasing temperature.[94] Therefore, thermoplastic polymers can be thermally liquefied, i.e. melted, at temperatures higher than their specific melting temperature. In this viscous configuration, they can be conveniently processed and shaped. In turn, with decreasing temperature these polymers solidify in the new shape.[94] This cycle of heating and cooling is reversible if no thermal degradation takes place.[95]

3.1.1. Polycaprolactone (PCL)

Poly(ε-caprolactone) (in this thesis also referred to as polycaprolactone or PCL) is a semicrystalline aliphatic polyester that is synthesized either by polycondensation of 6-hydroxyhexanoic acid or via ring opening polymerization of the cyclic ester ε-caprolactone under various catalytic regimes.[96] PCL is an established biomaterial with approval by various regulatory bodies for use in a wide variety of medical products and witnesses increasing research interest across a diverse field of applications and processing techniques.[97]

Bulk PCL has a Young's modulus of 250 MPa to 440 MPa, a tensile strength of 10 MPa to 27 MPa, and a strain at break of 80 % to 800 %.[98]

PCL is characterized by a relatively low melting temperature of ~ 65 °C and is stable at melting temperature over multiple days.[80,97,98] This, together with is flow properties (inherent viscosity of 1.2 dL g^{-1}) makes PCL particularly suited for MEW, resulting in the fact that PCL is to date the undoubted gold standard polymer for MEW.[99]

As with any polyester, PCL can degrade via hydrolysis of its ester bonds either via chemical or enzymatic pathways, with non-enzymatic, random chain scission being the major contributor in *in vivo* degradation.[100] Among other parameters, degradation rate depends on the temperature (increased temperatures generally lead to faster reactions), pH conditions (pH values below 3 and above 11 accelerate degradation),[101,102] as well as sample structure (geometry and cristallinity) and dimensions (determines the ratio of bulk degradation versus surface degradation).[98] Nevertheless, PCL is degrading

relatively slow (over 12 months and longer)[97,98,103] as compared to other biomaterials such as polyglycolic acid (PGA), poly D,L-lactide acid (PDLA), and poly D, L-lactic-glycolic acid (PLGA).[97,104]

3.1.2. Polydioxanone (PDO)

Polydioxanone (PDO) is a polyester, synthesized via catalyzed ring-opening polymerization of p-dioxanone.[105,106] After being introduced as first biodegradable surgical suture material in 1981,[107] PDO has been used also in other applications such as surgical meshes and plates.[105]

PDO has a slightly elevated melting temperature of ~ 105 °C compared to PCL[108] and its hydrolysis-driven degradation is much faster.[103,105] Also, PDO is far more sensitive to thermal degradation when in melt state,[48] hence requiring careful process design.

Bulk PDO shows a Young's modulus of ~ 500 MPa to 700 MPa, a tensile strength of ~ 45 MPa, and an elongation at break of ~ 160 % to 220 %.[109]

3.2. Fabrication Techniques

In this thesis additive manufacturing (AM) techniques are exploited to fabricate physical objects according to virtual models. ISO 52900 "Additive manufacturing - General principles - Terminology" defines AM as "*the process of joining materials to make objects from 3D model data, usually layer upon layer, as opposed to subtractive manufacturing methodologies*".[1] ISO 17296 "Additive manufacturing – General principles – Part 2: Overview of process categories and feedstock" classifies the plurality of AM processes in various categories as depicted in **Figure 3**.

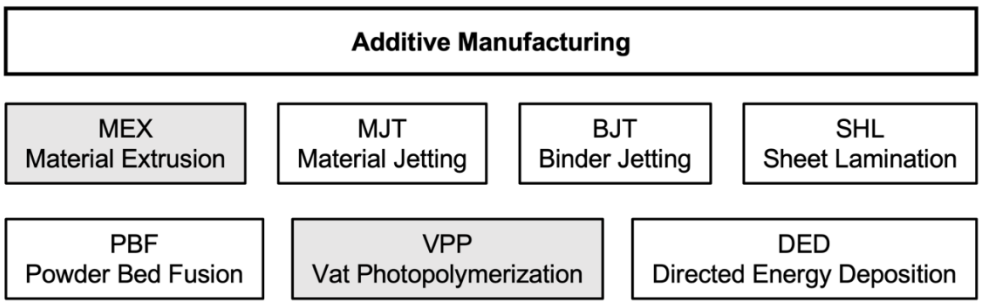

Figure 3: Classification of the AM processes according to ISO 17296. Techniques in the categories shaded in grey were applied or further developed in this thesis.

3.2.1. Melt Electrowriting (MEW)

Melt electrowriting is an extrusion-based AM technology and described in detail in sections 2.1 and 2.2. Briefly, MEW transforms an extruded thermoplastic polymer melt into a microfiber jet in the presence of a high voltage electrical field. This jet is deposited

onto a collector along computer-controlled pathways, where it cools down and solidifies. By repeatedly stacking multiple fiber layers, a highly ordered microfiber architecture can be formed.[6] The material library for MEW is still expanding as researchers are continuously exploring new materials as reviewed in detail elsewhere.[38,99] To date MEW is mostly used to fabricate scaffolds architectures for tissue engineering, ranging from hard tissues like bone to soft tissues like ligament, skin, and cardiovascular.[12] Furthermore, applications for e.g. sensors[110,111] and soft robotics[112] have also been reported.

3.2.2. Fused Filament Fabrication (FFF)

Fused filament fabrication (FFF) is a material extrusion AM technique that drives a thermoplastic filament via a pair of pinch wheels towards a so-called hot end, where the material gets liquefied and extruded.[5,77] While the filament acts as the piston driving the extrusion, it simultaneously serves as the feedstock material that is continuously replenishing itself.[5,77] Via a relative movement between print head and print bed the extruded material is deposited according to predefined toolpaths to form layered 3D structures.[5,77] While the feature resolution is limited by the nozzle diameter, which is typically not smaller than 150 µm,[78] parts resulting from FFF are usually in the range of centimeters but can range up to meters in the case of specialized machines for large area manufacturing.[113]

To date, the full range of thermoplastic polymers from low temperature melting polymers such as PCL up to high performance polymers like polyetheretherketone (PEEK) have been processed via FFF.[114,115] Particularly, semicrystalline thermoplastics and those with elevated melting temperatures require specialized machine components and a sophisticated thermal management of the FFF process, including full metal print heads as well as a heated print bed and print chamber, to enable adequate inter layer bonding and mitigate thermal stresses during cool-down that could lead to excessive warping.[116–118]

While thermal energy is primarily introduced to the FFF process via the polymer melt, heat losses occur via i) conduction from the part towards the print bed, ii) convection from the part towards the build volume, and iii) radiation (**Figure 4A**).[119–121] As radiation losses are minimal, FFF machines control and reduce conduction and convection heat losses via a heated print bed and print chamber to ensure sufficient time of the extruded polymer in the melt state and a controlled cool-down phase. In fact, bond formation between deposited filament strands is diffusion driven and as such dependent on both temperature and time.[114,122] Here, an initial surface contact between two neighboring

filament strands leads to necking with subsequent growth and diffusion of the polymer chains between the filament strands (**Figure 4B**).[114,122] These phenomena can also be translated to the layer stacking and bond formation of MEW fibers, however on a much smaller fiber scale and, hence, increased surface to volume ratio.

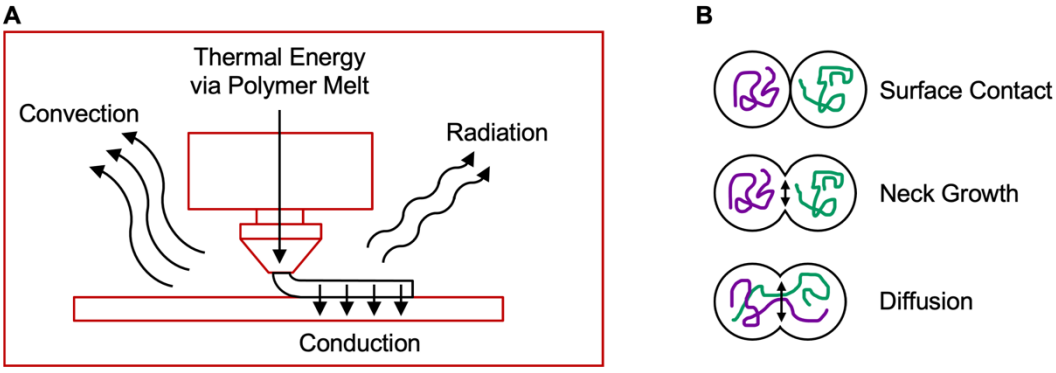

Figure 4: Schematic representation of the FFF process. A) In FFF, the polymer filament is heated in the print head. However, there are heat losses due to convection from the extruded polymer towards the build volume, conduction from the extruded polymer towards the print bed, and to a minor extent via radiation. To control these heat losses, both the build volume and print bed are heated (heated machine components indicated in red). B) Bond formation between deposited filament strands is a time and temperature dependent process, where after an initial surface contact, a neck starts to grow with subsequent diffusion of the polymer chains.

FFF is a widely established process in industry, academia, and the maker community, as its ecosystem provides readily configured workflows spanning the entire process chain from material selection, over process parameter design (slicing), to FFF systems with corresponding post-processing methods. Consequently, FFF has found its way into manifold applications, including biomedical.[123]

3.2.3. Stereolithography (SLA)

Stereolithography (SLA) belongs to the class of vat photopolymerization AM processes and exploits photopolymerization of photo-sensitive resins.[124] By selectively directing a light source (mostly UV light) into a resin bath contained in a vat, the desired cross-section of a part is cured onto a print bed to form a layer. Repeatedly curing individual layers forms a 3D component.[124] Photopolymers used for SLA usually consist of a mix of epoxy-based and/or acrylate-based monomers and oligomers, photoinitiators, as well as further additives, such as agents to avoid prepolymerization and to terminate the reaction as well as pigments.[125] Among a variety of resin compositions, there are also biocompatible resins available.[126]

The nozzle-free technology of SLA enables an exceptional resolution (~ 20 µm in XY plane), which mainly depends on the light source's spot size and the resin's reaction kinetics.[127] Together with a layer thickness in the 10 µm range, this positions SLA as an

excellent process for the fabrication of parts with intricate features and smooth surfaces for biomedical applications.[127]

3.2.4. Electroplating

Electroplating is a post-processing technique, which has in this thesis been used to coat polymer components with a metallic layer.[128] To this end, polymeric parts were first degreased and coated with a graphite spray to make them conductive. Next, the part to be coated is connected to the cathode of an external power supply, while a block of the coating metallic material serves as anode.[128] Both elements are submerged in an electrolyte solution that contains ions of the coating metal.[128] By providing an electrical current the metal ions travel towards the coating target and are deposited as thin layer, while the metal anode continuously replenishes the metal ions in the electrolyte solution. In this way, a net transfer of metal from the anode to the cathode target is realized.[128]

3.3. Biological Characterization

Every artificially produced implant is recognized by the human organism as foreign body. In this context D. Williams defined biocompatibility as "*the ability of a biomaterial to perform its desired function with respect to a medical therapy, without eliciting any undesirable local or systemic effects in the recipient or beneficiary of that therapy, but generating the most appropriate beneficial cellular or tissue response to that specific situation, and optimizing the clinically relevant performance of that therapy*".[129]

Constructs fabricated via MEW were tested for their effects of biological systems via various methods in agreement with the ISO 10993 "Biological evaluation of medical devices" family of standards. All tests require meaningful positive controls (PC) and negative controls (NC).

3.3.1. Cytotoxicity

Cytotoxicity describes the ability of a sample to harm cells and can be measured following ISO 10993-5 "Biological evaluation of medical devices - Part 5: Tests for *in vitro* cytotoxicity" to obtain both qualitative and quantitative metrics of the response of cellular systems to a material.[130] The tests can be performed either via extracts, via direct contact, or indirect contact of a cell culture with the sample material.[130] Latex can be used as PC and high density polyethylene (PE) as NC.[130]

To obtain extracts the material to be tested is incubated in culture medium with serum to leach potentially cytotoxic material components into the medium under specified extraction conditions (temperature and time) that should match those of the intended

application as indicated in ISO 10993-5.[130] The extract is later mixed to the culture medium of a subconfluent cell layer. Alternatively, cytocompatibility can be tested by placing the sample material directly on a subconfluent cell layer. Here, the sample needs to have at least one leveled surface that should cover 10 % of the cell layer. For indirect contact testing an agar layer or filter system is placed in between the cell layer and the sample material. This, however, comes at the disadvantage that particularly the agar might hinder diffusion of leachable substances towards the cell layer.[130]

After a defined culture time, the morphological conditions of the cells can be graded following levels indicated in ISO 10993-5.[130] Morphological changes equal or higher than level 3 (moderate) indicate cytotoxicity, where level 3 is reached when up to 70 % of the cell layer contains rounded or lysed cells.[130]

For a quantitative assessment tetrazolium salts can be added to the cell culture. These salts will be metabolically reduced to formazan in the active mitochondria of living cells and, therefore, this reaction is directly proportional to cell viability.[131] While MTT derivates of tetrazolium salts require an alcohol solution to be dissolved, XTT derivates are water-soluble and, therefore, allow metabolic monitoring at different time points. Formazan acts as dye so that a change in color of the culture medium can be quantified via the absorbance of light (usually 450 nm) in a photometer. A reduction of 30 % in metabolic activity in relation to the negative control indicates cytotoxicity according to ISO 10993-5.[130]

3.3.2. Hemocompatibility

Hemocompatibility can be assessed following ISO 10993-4 “Biological evaluation of medical devices - Part 4: Selection of tests for interactions with blood” by determining a material’s hemolytic potential, its effects on the coagulation time, and by quantifying the number of activated platelets adhering to the material.[132] For these tests different subcomponents of whole blood may be used. When whole blood is initially centrifuged, it separates into three layers from bottom to top in a centrifuge tube: the erythrocyte concentrate, a thin layer of leukocytes and platelets (also known as the buffy coat), and the (platelet rich) plasma.[133] When only the plasma layer (and eventually the buffy coat) is centrifuged again, this separates into a platelet concentrate at the bottom of the centrifuge tube with the platelet poor plasma on top.[133]

Hemolysis

Hemolysis describes the destruction of erythrocytes and can be quantified by photometrically measuring the amount of hemoglobin released from damaged erythrocytes.[134] To this end, the sample material is incubated with whole blood under

gentle agitation for a few hours. Whole blood diluted in distilled water can serve as PC, while whole blood diluted in saline solution can be used as NC. After centrifugation, a color change in the supernatants relative to that of the negative control indicates if there is a hemolytic potential. This color change can be quantified by measuring the absorbance at 545 nm in a spectrophotometer. The hemolytic rate is derived by calculating the difference in absorbance of the sample and that of the negative control normalized by the difference in absorbance of the positive control and that of the negative control. In general, a hemolytic rate of 5 % or less is classified as non-hemolytic.[135]

Coagulation Time

Measuring the coagulation time or plasma recalcification time is a metric to assess how fast the coagulation cascade is activated by the sample material.[136] Here, platelet-poor plasma from citrated whole blood is incubated with the sample material. Fibrin is a potential PC and pure platelet-poor plasma serves as NC. During incubation coagulation factors in the plasma are activated because of interactions with the material. Although this initiates the coagulation cascade, the cascade is interrupted as the previous citration renders Ca^{2+} unavailable, hence preventing the conversion of prothrombin into thrombin, which is in turn needed to convert fibrinogen into fibrin in order to complete the coagulation cascade.[137] It is only when Ca^{2+} is added to the solution again that the coagulation cascade can continue, which leads to an increased turbidity of the solution. This can be detected photometrically and the measured time between Ca^{2+} addition and onset of turbidity or the inflection point of the obtained curves serves as metric for the quantification of the coagulation time (**Figure 5**). Alternatively, the inflection point of the obtained curve or a predefined absorbance threshold value can be chosen to assess the coagulation time. As the obtained curves are only shifted along the time axis, these evaluation methods yield the same conclusion.

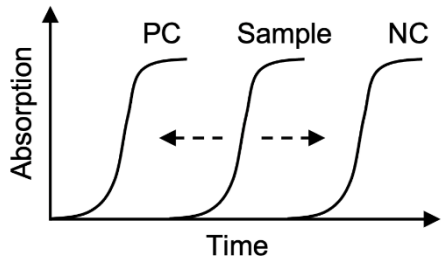

Figure 5: Schematic representation of absorption curves obtained via photometric measurements over time. Coagulation time can be defined at a threshold value of absorption or at the inflection point of the obtained curves. As the absorption curves are only shifted along the time axis, both evaluation methods yield the same conclusion. The closer the sample curve is to that of the negative control (NC) the longer the coagulation time is. Fibrin is often used as positive control (PC).

Platelet Adhesion and Activation

Adhering activated platelets play a crucial role in hemostasis and thrombosis.[138] While platelet adhesion and activation are the first steps of wound healing, this process can become also pathologic, when excessive thrombi are formed in response to an absent/dysfunctional endothelium.[139] While staining that specifically target activated platelets exist (e.g. CD 41, CD62P),[140] in this thesis platelet adhesion and activation was assessed using scanning electron microscopy (SEM, described below). To do so, the sample material is incubated with platelet rich plasma (PRP). After fixation, and preparation for SEM, the samples can be visualized and compared versus e.g. fibrin and expanded polytetrafluoroethylene (ePTFE) as reference materials. While non-activated platelets exhibit a disk-like shape, activated platelets form filopodia via actin polymerization resulting in a spread-out morphology.[141] Evaluating the surface area per image covered by activated platelets results in a quantitative metric.

3.3.3. Cellular Infiltration

Particularly *in situ* tissue engineering approaches critically depend on effective cell attachment and subsequent ingrowth.[84] The potential of scaffolds to allow for this trans-thickness migration can be evaluated via infiltration assays. To this end, scaffold samples are mounted in CellCrown inserts. These inserts are designed in such a way, that the scaffold is clamped in a flat manner, so that as a cell suspension is pipetted on the top-side of the scaffold, cell migration over the surface to the bottom-side is excluded. Thus, if cells are detected on the bottom-side, this indicates successful migration through the scaffold. After initial cell seeding, a waiting time allows for cell adhesion before the samples are entirely submerged in culture medium and further cultivated. At the time points of interest cultivation is stopped and the samples are fixated. After careful cutting, and preparation for SEM (including fixation in glutaraldehyde, washing, dehydration, and drying), the scaffold's cross-section can be visualized via SEM to examine the migration of cells along the scaffold's thickness direction over time.

3.4. Polymer Analysis

In this thesis polymers are modified by adding nanoparticles and pure polymers or polymer composites are processed into scaffold architectures via a variety of processes. The effects of these techniques on the resulting polymer or scaffold properties were examined via the following methods.

3.4.1. Inherent Viscosity

The inherent viscosity offers insights into the molecular size of a polymer and can, therefore, be used to estimate the progression of degradation. The inherent viscosity can

be determined by comparing the flow time of a polymer solution through a narrow capillary to that of the pure solvent, used for the polymer solution, flowing through the same capillary.[142] Longer flow times are related to longer molecular chains as these offer more entanglements which in turn restrict viscoelastic deformations.

3.4.2. Raman Spectroscopy

Raman spectroscopy is based on the inelastic scattering of monochromatic light.[143] As the photons interact with the vibrational modes associated with the chemical bonds within the sample, this results in an energy shift of the photons. [143,144] Hence, a so-called Raman spectrum can be recorded, where frequencies and their corresponding intensity provides information on the material composition of the sample with exceptionally high molecular specificity.

3.4.3. Tensile Testing

Tensile testing is a destructive method, that allows to characterize a material's force response in reaction to a controlled deformation. ISO 527 "Plastics - Determination of tensile properties" specifies sample geometries and test conditions for polymer materials.[145] While the typical sample geometry indicated by ISO 527 is the so-called dog-bone shape and intended for bulk material samples (e.g. injection molded),[145] this thesis used other samples geometries such as flat scaffold sheets. This is justified by the fabrication method of MEW, that in contrast to injection molding does not produce solid parts, but instead highly porous scaffold architectures with a small thickness as compared to their XY dimensions. Furthermore, tensile testing can be performed in a uniaxial manner or biaxially, where the deformation is applied in two orthogonal directions.

For tensile testing the sample is secured in between clamps which are mounted to linear stages. Next a deformation is applied at a controlled rate to the sample via the clamps and the resulting force response is recorded. Testing can be performed in a cyclic manner and/or until failure

The engineering strain is calculated by normalizing the change in gauge length by the initial gauge length.[146] The engineering stress is derived by dividing the recorded force by the nominal cross-section of the sample, which must be measured before the test.[146]

Plotting stress over strain results in a stress-strain curve from which the following key characteristics can be derived (**Figure 6**). Yield strength describes the stress at which the material changes from an elastic elongation mode into plastic deformation. This point usually marks the end of the initial linear section of the stress-strain curve. In this linear

section the Young's modulus, also known as modulus of elasticity, can be calculated as indicator of a material's stiffness by dividing the strain difference by the stress difference. This calculation is ideally performed using a line of best fit instead of taking start and end points of the linear section only to avoid falsified results due to data outliers. Ultimate tensile strength (UTS) is defined as the maximum stress a sample can hold before the stress-strain curve may decline again. Stress at break is derived from the last point of the stress-strain curve where the sample ultimately failed. Even if this value is higher than UTS is not recorded as maximum force as per ISO guidelines to avoid flickering of the results between UTS and stress at break within in a sample group.[145] All stress values are designated with corresponding strain values, e.g. yield strain, strain at break.

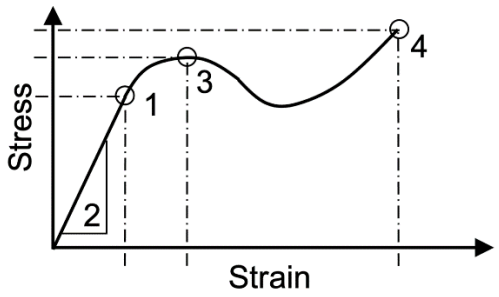

Figure 6: Stress-strain curve typical of a thermoplastic material. Elastic deformation takes place until yield (1). In the linear elastic region, the Young's modulus (2) can be derived from the slope of the curve. Ultimate tensile strength (3) is defined as maximum stress before the stress may decrease again. While some polymers break near UTS, others might undergo significant further strain until they ultimately fail (4).

It is important to note that polymers show a strain rate-dependent and temperature-dependent mechanical behavior, with the general trend that higher strain rates lead to a stiffer response, while higher temperatures result in lower stiffness.[147]

Setups for tensile testing can easily be modified to also perform related methods, such as suture retention. Here, a surgical suture line is introduced in the sample and attached to one of the clamps while the sample is immobilized in the opposite clamp. By applying a change in gauge length, the suture line is pulled through the sample, and the sample's resistance against tearing can be assessed from the resulting force curve.

3.5. Imaging Methods

This thesis applied various imaging methods to visualize both macrostructural and microstructural features of MEW constructs and interactions between materials, cellular systems, and fabricated samples.

3.5.1. Optical Microscopy

Optical microscopes build on the interaction of visible light with a sample to visualize a magnified view of an object. Such microscopes can be divided in two groups, namely reflected-light microscopes, where only reflected light is used to visualize the sample, and transmitted-light microscopes, where the light is travelling through the sample and translucent samples are required.

Magnification describes the ratio of the apparent size of the image and the true size of the object. Optical microscopes use multiple glass lenses to obtain a virtual magnified image. To do so, the object is placed outside the focal length of the objective lens, hence an inverted magnified intermediate image is generated. This image in turn, is positioned within the focal length of the ocular lens, which consequently creates a further magnified virtual image, which is received by the human eye. An optical microscope's total magnification can be calculated by multiplying the magnification of the objective with that of the ocular.[148] Optical microscopes typically achieve a magnification of up to 1000x.

Resolution defines the minimum distance between two physical structures that can be perceived as separate elements after optical imaging.[148] The use of visible light in optical microscopes limits their resolution, which *inter alia* depends on the wavelength of light, to the range of 200 nm to 400 nm.[148,149]

Another important aspect is the achievable depth of field, which in contrast to resolution, refers to the maximum distance in Z-direction between the nearest and furthest objects in focus within an image. This measure describes the 3D impression of an image and is for optical microscopes in the range of 400 nm to 900 nm.[148]

Optical microscopes can be enhanced with digital functions, such as image stitching to produce larger total images from multiple magnified subimages, or focus stacking, where only selected areas in focus of multiple subimages taken at different focus levels are combined to result in a single image with increased depth of field.[150]

3.5.2. Fluorescence Microscopy

Fluorescence microscopy leverages the effects of excitation and emission of fluorophores. Fluorophore probes are chemical compounds that can be excited by absorbing a photon with sufficient energy to enable transition of an electron to a higher electronic state. Upon returning to the ground state, the electron releases excess energy by emitting a photon of lower energy than that of the exciting light (Stokes-shift).[151] It is exactly this shift in energy (and wavelength) that enables fluorescence microscopy by

filtering out the exciting light by wavelength without blocking the emitted fluorescence signal.

Cellular components can be tagged with fluorophores following specific staining protocols. In short, two pathways exist to bind fluorophores to their target. Some fluorescent dyes show direct affinity, such as DAPI that binds to adenine–thymine-rich regions in the DNA or fluorophore-conjugated phalloidin that interacts with the actin filaments of the cytoskeleton.[152,153] The second class of fluorophore probes binds via the antibody-antigen principle.[154] This enables the detection of specific proteins inside and in the vicinity of cells. Multiple fluorescent dyes can be added to a sample, to visualize various structural elements within a single image.

Fluorescence microscopes are optical microscopes equipped with an excitation filter, through which only wavelengths can pass that are suitable to excite the desired fluorophore, and an emission filter, that blocks unwanted traces of excitation light. To separate the light paths for excitation and of emission, a dichroic mirror reflects the light of shorter wavelength towards the sample, while letting the light of higher wavelength pass towards the detector.[151]

3.5.3. Scanning Electron Microscopy

Scanning electron microscopy (SEM) uses an electron beam to visualize samples. As electrons have a wavelength up to ten thousand times smaller than photons of visible light, the resolution achieved by SEM, typically between 1 nm and 10 nm, is far higher than that of optical microscopes.[149,155]

Electron beams can be generated via so-called electron guns, where electrons are emitted from a cathode via thermionic emission and accelerated towards an anode.[149] Here, the accelerating voltage defines the electrons' wavelength and hence the resolution. In contrast to glass lenses in optical microscopy, electron microscopy uses electromagnetic lenses that interact with the electron beam to first focus it via condenser lenses and next manipulate the electron beam via deflection lenses to scan the sample surface.[155] To prevent scattering events of the electrons during their travel towards the sample electron microscopy is usually performed under vacuum.

Multiple interaction mechanisms of the electrons with the sample material exist and can be recorded to generate images containing various information on the sample's surface morphology or composition. Most commonly, secondary electrons are collected. These electrons are ejected from the atoms of the sample via inelastic scattering interactions with beam electrons. Due to their low energy, these electrons originate from the sample surface and hence provide topological information.[149]

Alternatively, backscattered electrons can be collected to generate images. These are high-energy electrons originating from the electron beam, which were reflected or backscattered by elastic interactions with the sample's atoms, specifically their positively charged nuclei. This modality enables insight into the sample composition, as heavy elements backscatter electrons more strongly than light elements do.[149]

Furthermore, energy-dispersive X-ray spectroscopy can be performed to assess the elemental composition of a sample. This builds on the concept, that the electron beam can displace a sample electron in an inner shell (so-called knock-out electron) thus leaving an electron hole. Once an electron from a higher-energy outer shell relocates to fill the electron hole, surplus energy is released in the form of an X-ray. As each element is characterized by a unique emission spectrum, the sample's elemental composition can be identified.

To enable interaction of the electron beam with the sample surface and to prevent the buildup of charges, the sample must be electrically conductive. In case of polymeric samples, this can be achieved by sputter coating the surface with a metallic layer. Also, wet samples, as e.g. those from cell culture, need to by dried, e.g. via chemical drying steps or critical point drying, to avoid pollution of the vacuum during imaging.

3.5.4. Computed Tomography

Computed tomography (CT) is a non-invasive imaging method based on X-rays.[156] Conventional X-ray radiography visualizes a 3D object via a 2D projection. While this approach allows to visualize hard tissues like bone, it does not provide sufficient contrast for soft tissues.[157] On the contrary, in CT multiple projections from various imaging angles are superimposed to obtain increased contrast.[156] To this end, the X-ray source is moved relatively to the detector while circling the sample. Interactions of the X-ray with the sample lead to attenuation of the detected signal, which can be visualized in grey values (and e.g. later sorted per tissue type using the Hounsfield scale).[157] Because of the relative movement of the X-ray source versus detector, central image elements are sharp with increasing blurring toward the outside.[156] The sum of attenuation values per projection angle represents the image data in the so-called Radon space.[156] Via mathematical operations including a Fourier transformation a 3D representation of the sample can be reconstructed, therefore, providing volumetric information, such as internal composition and structure.[156]

3.5.5. Magnetic Resonance Imaging

Magnetic resonance imaging (MRI) is a radiation-free imaging technique that exploits the phenomenon of nuclear magnetic resonance. An MRI scanner positions the sample in a

strong constant magnetic field, to which those atomic nuclei with a spin react paramagnetically by reorienting within the magnetic field.[158] When a second, alternating magnetic field is applied, the orientation of these nuclei is disturbed and the nuclei react with a Larmor precession, which in turn induces an electric signal that can be recorded by a receiver coil.[159] Once the second magnetic field is deactivated, the atomic nuclei return to their initial orientation in the constant magnetic field. This relaxation takes place in both longitudinal and transversal direction, resulting in a longitudinal (T_1) and transversal (T_2) relaxation time.[92] The difference in the rate of relaxation of the nuclear spins and their density is recorded und used to generate contrast in an image. The characteristics of the pulse sequence of the alternating magnetic field determines which of these parameters (T_1, T_2, nuclei density) effects the image contrast.[158]

Due to their natural abundance hydrogen nuclei (^1H) are usually imaged, however other nuclei such as ^{19}F can also be targeted.[160] Contrast agents can be used to increase contrast in MRI, by modulating the response of the nuclei (higher or lower relaxation rate) to the alternating magnetic field.[92]

3.6. Characterization of Vascular Grafts

Next to biocompatibility, as described above, vascular grafts are to be mechanically characterized as indicated in ISO 7198 “Cardiovascular implants and extracorporeal systems”.[161] A selection of tests of ISO 7198 has been performed in this thesis and is outlined below.

3.6.1. Compliance

Compliance describes the radial extensibility of a graft in response to a pulsatile luminal pressure profile.[161] Compliance can be measured with the help of an optical micrometer. To this end the graft is positioned within the light beam of the optical micrometer and subjected to a pulsatile pressure profile. By measuring the change of the graft’s shadow dimensions, the variability in diameter can be recorded and correlated to the corresponding pressure value. ISO 7198 indicates a minimum graft length of ten times the graft’s diameter and a pressure profile of 60 ± 10 pulses per minute between with 80 to 120 mmHg, 50 to 90 mmHg, and 110 to 150 mmHg as test conditions. Highly compliant liners can be inserted in the graft to avoid leaking during testing.[161]

Alternatively, ring tensile tests can be performed and La Place’s law used to indirectly calculate the compliance.[162]

3.6.2. Burst Pressure

The burst pressure defines the maximum pressure, which the graft's wall can be subjected to before it fails due to mechanical disintegration. To this end, a sample element is fixed within a chamber where a pressure is applied to one side of the sample. Next, the pressure is gradually increased until failure is recorded. The peak pressure before disintegration of the sample is taken as burst pressure. To pass this test ISO 7198 requires a burst pressure significantly higher than 120 mmHg.[161]

3.6.3. Kinking Radius

Assessing the kinking radius serves to determine the minimum bending radius of the graft without considerable reduction of the luminal diameter.[161] This can be quantified by bending a graft around templates with decreasing radii, while being pressurized to 100 mmHg luminal pressure. The outer diameter of the bent graft is measured from photograph and under assumption of a constant wall thickness (as in the unloaded straight graft) the luminal diameter is calculated. A reduction of 50 % or more of the luminal diameter with respect to the straight graft is defined as kinking.[161]

3.6.4. Suture Retention Force

The suture retention force describes the resistance of a material against pulling a suture through the graft's wall.[161] This is assessed by inserting a suture loop 2 mm from the end of the graft and while the graft is immobilized, the suture line is pulled while recording the force response (e.g. by using a tensile testing machine as described in section 3.4.3.). The maximum force before failure of the graft's wall is taken as the suture retention force.[161]

4. Design and Fabrication of a Syringe-based Melt Electrowriting System

The content of this chapter is based on:

Paulina Kraus, *Development and Validation of a Melt Electrowriting Setup*, Master's Thesis, TUM School of Engineering and Design, Technical University of Munich, 2022.

Kerstin Janocha, *Development of a Closed-loop Kinematic for Melt Electrowriting onto Flat or Tubular Collectors*, Semester Thesis, TUM School of Engineering and Design, Technical University of Munich, 2024.

Kilian M.A. Mueller provided the central ideas and concepts that were developed and reported in these theses under his direct supervision.

4.1. Introduction

Two different MEW machines were developed to establish MEW as one of the central research lines at the chair of Medical Materials and Implants.

This chapter outlines the design of the complete MEW printers. This includes print head design for syringe-based MEW using plastic syringes (for polymer melt temperatures up to 110 °C) or glass syringes (for polymer melt temperatures up to 220 °C). Furthermore, the design of a flat collector with integrated thermal control as well as a system to mount tubular collectors with up to 35 mm diameter is reported. The print head and collectors are integrated into either a commercially available kinematic system or, alternatively, in an in-house configured one, both offering closed-loop positioning. To ensure safe user operation, the MEW set-ups feature a housing with a safety door interlock to interrupt the high voltage once the door is opened.

4.2. Syringe-based Print Head

The print head assembly for syringe-based MEW (**Figure 7**) consists of a syringe heating zone and needle heating zone and can be mounted to the Z-axis of the kinematic system using a set of adapters. Letter tags in the following text refer to those indicated in **Figure 7A**.

The print head features a cylindrical body with a cartridge (R) containing the feedstock polymer positioned in the lumen of a Shapal ceramic cylinder (O) that is custom fabricated by Schröder Spezialglas, Germany. Shapal is an aluminum nitride ceramic with excellent thermal conductivity and high electrical insulating properties. This cylinder features additional circumferentially aligned holes to host a thermosensor (8600210, Hotset, Germany) and three heating cartridges oriented in parallel with the syringe axis, which were controlled via a two-zone temperature controller (MI8844820G, Hotset, Germany). This assembly is sitting inside a PTFE cylinder (P) and is forming the syringe heating zone. The main body of the needle heating assembly (M) is also fabricated from PTFE and is attached to the bottom of the syringe heating zone via six PA screws. It houses a H-shaped brass element (G) that perpendicularly to the needle axis in which two heating cartridges (F) with an integrated thermosensor (hotrod MIUE04003F, Hotset, Germany) are located. The H-shaped brass piece is electrically grounded. A layer of Kapton film (K) (CMC70849, CMC Klebetechnik, Germany) electrically insulates the H-shaped brass element from a flat brass disk (electrode) (J) which is in contact with the needle (N) of the syringe and to which one polarity of the high voltage electric field is

applied via a high voltage power source (MPL 200-30000 POS, FuG Elektronik, Germany). Pressurized air can be applied to the syringe via an electropneumatic regulator (ITV1050-31F1CL3, SMC, Japan). Adjusting the inner dimension of the Shapal cylinder allows to work with either plastic syringes (3cc Optimum, Nordson EFD, USA with precision tip 23 G, Nordson EFD, USA) until up to 110 °C operating temperature or glass syringes (Fortuna 3 ml, Poulten & Graf, Germany) and metal needles (23G injection needle, Carl Roth, Germany) if higher operating temperatures (up to 220 °C) are required. In the latter case, the PA screws need to be replaced by PEEK screws.

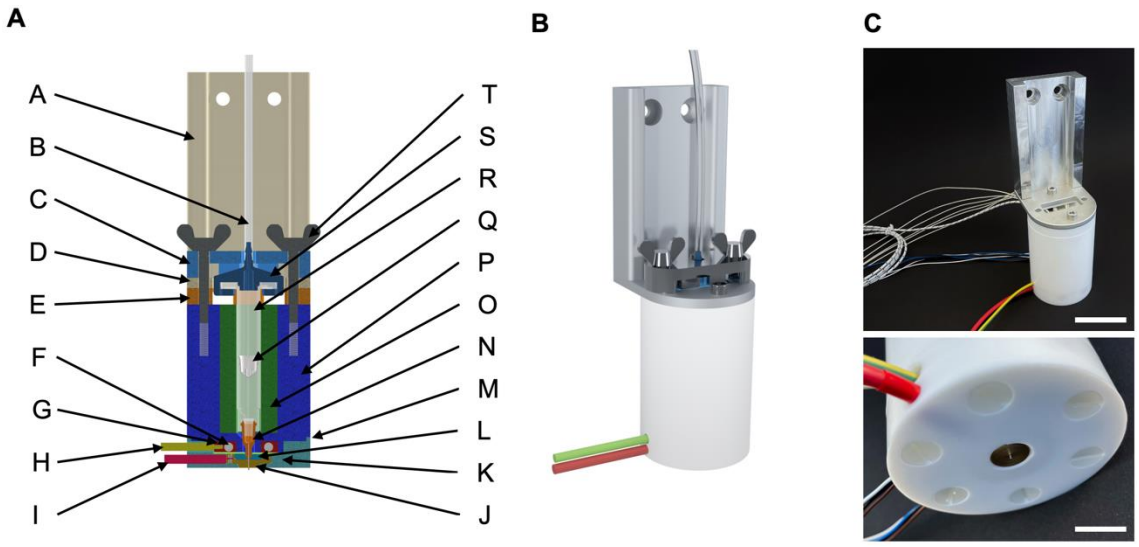

Figure 7: Print head for syringe-based MEW. A) Sectional view through the CAD design in false coloring with the following components: A: aluminum adapter to Z-axis, B: pressurized air hose, C: aluminum syringe clamp, D: aluminum adapter to part A, E: PTFE spacer, F: heating cartridge, G: H-shaped brass piece, H: grounding cable, I: high-voltage cable, J: brass electrode, K: Kapton tape, L: PTFE inlay, M: PTFE main body needle heating zone, N: needle, O: ceramic cylinder, P: PTFE main body syringe heating zone, Q: syringe plunger, R: plastic syringe, S: syringe adapter, T: wing screws. Note: heating cartridges and corresponding thermosensor are not visible in this sectional view. B). Rendering of the print head as assembled on the machine. C) Photograph of the print head assembly (without syringe) with cables for the thermal management leaving from the print head's back side and the grounding cable and HV cable on the left side (scale bar 10 cm). Bottom view of the print head highlighting the brass electrode from which the needle tip is protruding about 0.5 mm (scale bar 2 cm).

4.3. Collector

The collector assembly is based on a flat print bed design which provides a print area of 20 cm by 20 cm. MEW machine is equipped with a flat collector and a rotating holder for tubular collectors. Letter tags in the following text refer to those indicated in **Figure 8A**.

The flat collector consists of an aluminum plate (B) to which a silicone heating mat (C) (FF-SHM-200200-24V-200W, Filafarm, Germany) with an integrated thermistor type 100K - 3950 is glued (**Figure 8**). The temperature of the heating mat can be controlled to maximum 150 °C via a thermostat (ED330L, Zhongshan Shangfang Instrument Meter, China). The heating mat is separated from the remaining collector components via

silicone frame (D). This provides an air gap to direct the generated heat into the aluminum plate and not into the PC plate (E) that connects the assembly to the axis adapter. The adapter is made from a PVC plate (F) and a POM block (G) to be mounted onto the Y-axis.

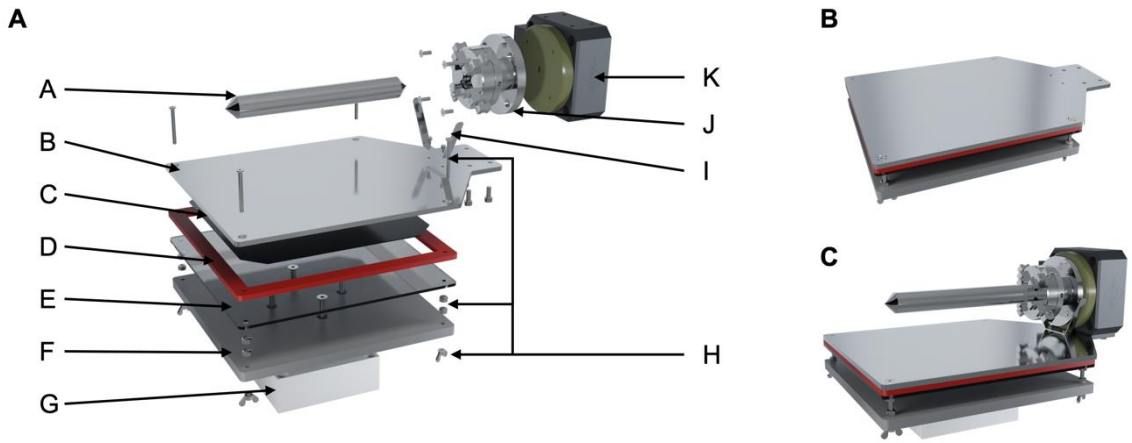

Figure 8: Collector assembly for flat and tubular MEW. A) Rendering of the collector assembly with the following components: A: cylindrical collector of up to 35 mm diameter, B: aluminum plate, C: silicone heating mat, D: silicone spacer frame, E: PC plate, F: PVC plate, G: POM adapter block, H: leveling screws and nuts, I: grounding clamp for tubular collectors, J: 4-jaw chuck with adapter to K: rotational motor. B) Rendering of the collector assembly for flat MEW. C) Rendering for the assembly for tubular MEW.

To enable tubular MEW, the 4-jaw chuck flange (J) allows to mount cylindrical collectors of up to 35 mm diameter. The collector assembly can be leveled via four screws (H) located at its corners. The electrical ground is applied to one of the screws and via a grounding clamp (I) continued to the cylindrical collectors.

4.4. Kinematic System

The collector assembly is mounted to the Y-axis of an X-Y cross-table axis configuration. In this, two separate MEW printers were developed. For the first one a readily configured commercial kinematic system of three linear mechanical-bearing screw-driven stages (PRO115SL-300-M1-3-LI1-CP1-PL2-TAS, PRO115SL-300-TT1-M1-3-LI1-CP1-PL2-TAS, and PRO115SL-150-TT1-M1-3-LI1-CP1-PL2-TAS, Aerotech, Germany) and one direct-drive rotary stage (ADRS100-E6-M1-TT1-PL2-TAS, Aerotech, Germany) was used. The X and Y linear stages cover a travel length of 300 mm, while the Z-axis is configured for 150 mm travel length. All axes feature closed-loop positional control resulting in a bidirectional accuracy of ± 1 µm and ± 14.5 µrad for the linear and rotational axes, respectively. Gcode commands can be loaded and executed via the software Automation1 Studio (Aerotech, Germany) running on an iPC (Aerotech, Germany).

For the second MEW machine, a kinematic system was configured in-house. This system consisted of a cross-table X-Y assembly (PSK-050-NN-1, ball screw-driven, travel length 313 mm, Bosch, Germany) and an orthogonal Z-axis (PSK-050-NN-1, ball screw-driven, travel length 170.3 mm, Bosch, Germany). The axes were actuated via stepper motors with integrated encoders (Nema 17, 17E1K-05, Stepperonline, China) to enable closed-loop control. Tubular MEW was enabled by mounting a stepper motor together with an in-house developed gear system of 1:3 onto the flat collector assembly. To this end, the stepper motor was equipped with a 20T pulley wheel, that was connected to a 60T pulley wheel sitting on an in-house developed spindle using a GT2 timing belt. The 4-jaw chuck was mounted to the spindle. The motors were controlled via a Duet3 Mini5+ Ethernet (Duet3D, United Kingdom) with a Duet 3 Expansion Board (1HCL V1.0, Duet3D, United Kingdom) for each stepper motor. Gcode commands can be uploaded to the Duet board via the web interface.

4.5. Housing

The housing serves the main purpose of shielding operators from the potentially hazardous high voltage. It additionally provides the frame to mount the kinematic system and to host most of the platform's components (**Figure 9A**). It consists of a cubic frame from aluminum profiles (40 x 40 mm, Nut 8, 7.0.000.09, ITEM, Germany) with acrylic panels as windows. With its external dimensions of 920 mm x 800 mm x 800 mm (H x W x L) it fits onto standard lab tables (**Figure 9B**). An internal portal serves as mount for the Z-axis. A door at the front side enables the operator to access the machine. The door is equipped with a potential-free magnetic switch (XCSDMP5912, Schneider Electric, Germany) that shuts down the high voltage output when the door is opened to protect the operator. All elements of the housing and kinematic system were grounded using earthing terminals (0.3.001.81, ITEM, Germany).

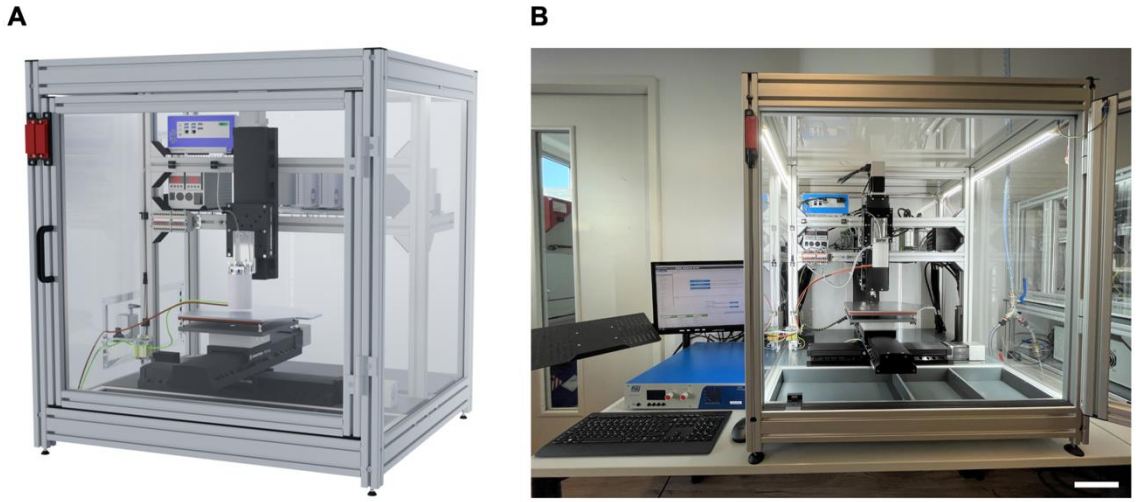

Figure 9: Fully assembled platform configured for flat MEW. A) Rendering of the MEW platform with iPC and the two-zone temperature controller located in the rear left. The Z-axis carrying the print head was mounted on the aluminum frame portal and the X-Y cross-table with collector assembly was mounted onto the base frames of the housing. B) Photograph of the fully assembled MEW platform showing also the high voltage power supply and the operator screen on the left of the system (scale bar 10 cm).

5. Filament-based Melt Electrowriting Enables Dual Mode Additive Manufacturing for Multiscale Constructs

Kilian M. A. Mueller*, Annika Hangleiter*, Sarah Burkhardt, Diana M. Rojas-González, Christina Kwade, Sebastian T. Pammer, Stefan Leonhardt, Petra Mela
* equal contribution

Small Science 3:8, 2023

Supporting materials associated with this article can be found in the online version at DOI: 10.1002/smsc.202300021

Conventional MEW systems build on syringe-based print heads, where the entire feedstock material is melted and pneumatically extruded, mostly via pressurized air. Due to the low flow rates (~ µL h^{-1}) required during microfiber fabrication, the entire feedstock material is subjected to melting temperatures for extended periods of time, often over weeks, hence placing a significant thermal burden to the polymer. Furthermore, syringe-based print heads require custom-designed and complex machine components, which significantly decrease accessibility of MEW to a larger user group.

In contrast to the conventional syringe-based design, a filament-based approach to MEW (F-MEW) is presented. Here, a thermoplastic filament is driven via a pair of pinch wheels to the print head, where it is melted just on demand. This concept modifies machine components from the ubiquitous FFF technology ecosystem, hence potentially opening F-MEW to a large user community. In this study, F-MEW is enabled by grounding the FFF nozzle and applying the polarity of the high-voltage electric field to a custom-designed collector that can be placed onto the print bed of an FFF printer. No further modifications of a standard FFF printer are required.

The F-MEW system was validated by fabricating both linear and non-linear stacked fiber patterns and by producing PCL microfibers with consistent diameters from 10.7 ± 0.5 µm to 33.8 ± 1.4 µm. Attachment of human umbilical vein endothelial cells (HUVECs) to the F-MEW PCL microfibers was successfully verified via fluorescence imaging.

Furthermore, the melt-on-demand approach allowed to melt electrowrite, for the first time, the thermosensitive polymer polydioxanone (PDO) into accurately stacked box-pore scaffold designs.

As the FFF mode of the modified printer was still fully functional, multiscale additive manufacturing was demonstrated by fabricating i) macrostructures via FFF, that ii) were decorated with microfibers via F-MEW. HUVECs, that were seeded onto the multiscale scaffolds, wrapped around the F-MEW microfibers, while they spread out on the large FFF fibers as visualized via fluorescence imaging.

This work opens new avenues towards multiscale additive manufacturing by combining FFF and F-MEW in a single print head, requiring only minor modifications to components of the widely established FFF ecosystem. Therefore, F-MEW significantly lowers the entry barrier for new user to start exploring microfiber architectures, while also enabling the processing of thermosensitive polymers.

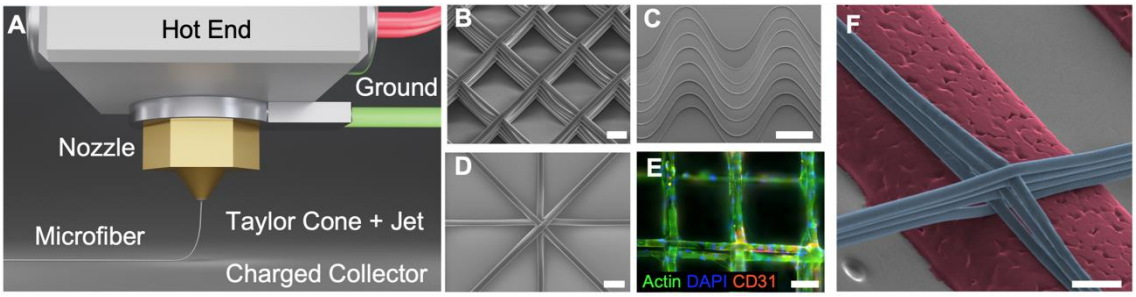

Figure 10: Table of content graphic: Filament-based MEW. A) Electrically grounding a standard FFF print head and applying the high voltage to a custom-designed collector, enabled electrohydrodynamic writing of polymer melts. B, C, D) The concept was validated with PCL multilayered linear and non-linear fiber patterns (scale bars 100 µm, 500 µm, 500 µm). Furthermore, cellular colonization was shown with E) HUVECs wrapping around PCL fibers after three days of culture (scale bar 100 µm). F) By exploiting the melt-on-demand nature of F-MEW, the thermosensitive polymer PDO could be processed, and dual-mode multiscale constructs were fabricated. FFF struts are shown in red and F-MEW fibers in blue (scale bar 100 µm).[48]

Contribution statement of **Kilian M. A. Mueller**: conceptualization, data curation, formal analysis, funding acquisition, investigation, methodology, software, validation, visualization, writing – original draft, writing – review and editing.

6. A Versatile 5-Axis Melt Electrowriting Platform for Unprecedented Design Freedom of 3D Fibrous Scaffolds

Pietro Terranova*, **Kilian M. A. Mueller***, Dominic Biebl, Antonio D'Amore, Petra Mela
* equal contribution

Additive Manufacturing 93, 204

Supporting materials associated with this article can be found in the online version at DOI: 10.1016/j.addma.2024.104431

To date MEW systems only exploit the motion of three simultaneously operating axes to fabricate either flat scaffold geometries by using three translating axes (X, Y, and Z) or tubular architectures by combining the motion of two translating axes (X and Z) with the motion of a rotatory axis (U). Approaches towards "out-of-plane" MEW were so far limited by printing onto 3D molds placed on flat collectors or onto tubular collectors with varying diameters. These studies clearly showed the challenge of providing constant electric field conditions to avoid distortions in fiber deposition. Furthermore, the only attempt to exploit a 6-axis robotic arm for melt electrowriting onto a spherical collector had failed, as a relative motion consistently above the critical translation speed could not be achieved.

In this work, a 5-axis kinematic system is presented, that together with a novel print head design enables MEW onto multicurvature collector geometries with a freedom of design unconceivable with current MEW technology.

To this end a 3-axis kinematic system (X, Y, and Z) of a commercially available FFF printer is upgraded with two additional rotating axes (U, V). Furthermore, the components to enable a high voltage electric field for MEW are integrated into that 5-axis systems.

Additionally, a novel design for a syringe-based MEW print head is outlined, which reduces the 3D footprint of the print head, hence enabling increased clearance. This results in the accessibility of narrow collector concavities and allows collision-free positioning. The print head design featured a needle that protruded about 25 mm from the main body, and therefore, required a dedicated inhouse-developed heating system, to avoid early solidification of the polymer and nozzle clogging.

As MEW is inherently bound to deposit the microfiber jet onto a collector, a workflow to fabricate arbitrarily shaped collectors is presented. This workflow builds on the additive manufacturing technique stereolithography to produce custom-designed collector templates, that were, subsequently, copper-coated via electroplating to achieve an electrically conductive collector surface.

Next, a graphical approach to generate Gcode for complex motion commands is outlined. This is based on virtually sketching the desired fiber pattern onto a digital representation of the collector in Rhinoceros. This is then transformed into Gcode for 5-axis motion via a Grasshopper script plugin. The inverse kinematics of the Grasshopper script ensures that the needle is always positioned orthogonally to the collector's surface at a constant working distance. This graphical approach to generate Gcode is universal and also accessible to users without prior knowledge on Gcode programming.

The 5-axis MEW platform was validated by printing both linear and non-linear patters onto a collector featuring a convex and concave side. Fiber diameters ranging from 5.6 ± 1.7 µm to 50.7 ± 5.5 µm were produced and accurate fiber position in agreement with the planned fiber architecture was verified. Successful stacking of up to 20 layers was demonstrated.

To highlight the platform's potential for the fabrication of anatomically relevant microfiber architectures, reinforcement patterns for trileaflet valves were fabricated near-net-shape onto an anatomically correct collector. This collector geometry featured both radial and circumferential concavities, hence, requiring simultaneous motion of all five axes.

Lastly, a scaffold of a bifurcating vessel graft was fabricated on a collector featuring two daughter vessels branching from the main vessel at different angles. Hence, this collector geometry featured more than a single axis of rotation. Melt electrowriting onto such a geometry requires 5-axis motion to avoid collisions. To release the scaffold after fabrication, the collector can either be carefully cracked. Alternatively, a collector consisting of an assembly of the main vessel and the daughter vessels, can be carefully disassembled.

In conclusion, this work unlocks unprecedented freedom of design for complex anatomically relevant scaffold geometries.

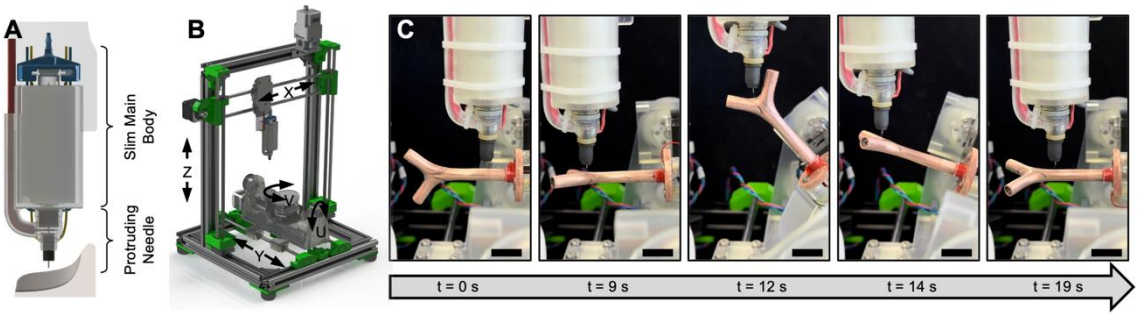

Figure 11: Table of content graphic: 5-axis MEW. The new low-cost, versatile platform includes A) a small foot-print head for increased clearance, B) a conventional FFF kinematic system augmented to five axes and a universal Gcode generator to enable unprecedented freedom demonstrated with C) the fabrication of a bifurcated vascular scaffold (scale bars 1 cm).[163]

Contribution statement of **Kilian M. A. Mueller**: conceptualization, data curation, formal analysis, funding acquisition, investigation, methodology, software, validation, visualization, writing – original draft, writing – review and editing.

7. Advances in Melt Electrowriting for Cardiovascular Applications

Kilian M. A. Mueller, Salma Mansi, Elena M. De-Juan-Pardo, Petra Mela

Frontiers in Bioengineering and Biotechnology 12, 2024

DOI: 10.3389/fbioe.2024.1425073

Melt electrowriting (MEW) is attracting increasing interest as versatile biofabrication technique across a wide range of tissue engineering applications, including *inter alia* bone, cartilage, ligament, neural, and skin. This is due to the targeted microfiber placement of MEW, which allows for bioinspired scaffold designs. This review summarizes the advances of MEW as technology platform for cardiovascular applications, specifically i) microvascular networks, ii) small diameter vascular grafts, iii) cardiac patches, and iv) heart valves. Furthermore, material and technology challenges relevant to cardiovascular tissue engineering are discussed.

Artificially produced thick tissues show limited oxygen diffusion and, therefore, crucially rely on a capillary network to supply nutrients and remove metabolic waste. The recreation of such microvascular networks is a major challenge in the TE field. By embedding sacrificial MEW microfibers into a matrix (e.g. cell-laden hydrogels) and subsequent postprocessing steps, microchannels were accurately templated. Here, solution-based removal processes (e.g. for water-soluble isomalt) are reported as well as physical removal of the fibers by pulling them out of the matrix. It is particularly the solution-based approaches that allow for the fabrication of complex bifurcating microchannel networks.

Cardiac patches hold the potential to repair infarcted myocardial tissue. To this end, they should be capable of i) sustaining large strains of the cardiac muscle, ii) supporting myocardial electroconductivity, and II) delivering cells and growth factors to the infarcted area. Here, various scaffold architectures were exploited to store elastic energy (hexagonal designs) or to allow for large strains (auxetic designs). Furthermore, material coatings were explored to enhance the electrical conductivity of polymer microfibers and the development of contractile minitissues was investigated reported.

Autologous and synthetic vascular grafts are an integral tool of vascular surgery. However, tissue-engineered small diameter vascular grafts have not yet reached the clinic. On an architectural level, studies report the investigation of linear fiber patterns to guide cell alignment similar to that in the vessel wall or sinusoidal patterns to enable compliant vascular grafts. Various studies report the combination of electrospinning with MEW to obtain biomimetic vascular grafts for *in situ* tissue engineering, while also the *in vitro* tissue engineering approach is demonstrated using purely melt-electrowritten scaffolds.

Heart valves show complex mechanical properties, including anisotropy and a non-linear stress-strain response, as well as spatial heterogeneity. In this context MEW excels with is capability to fabricate complex bioinspired scaffold designs. Scaffold architectures of alternating arcs were developed to recapitulate the native J-shaped stress strain response and anisotropy (radial versus circumferential direction). Furthermore, a tubular trileaflet scaffold design was presented that featured a wavy fiber architecture in the leaflet areas while a linear pattern was exploited for the interleaflet triangles. Other work points to the importance of engineering interfaces between regions of different patterns to avoid zones with the potential for onset of mechanical failure.

Furthermore, combinations of MEW with other biofabrication techniques are showcased to show the potential of hybrid biofabrication approaches to mimic the complexity of native tissues. Also, attempts to achieve scaffolds geometries with higher complexity than flat and tubular designs are reported. Lastly, we point to material advances that enhance antibacterial activity, enable imaging of MEW fibers, and methods for cytokine and drug loading of melt-electrowritten microfibers.

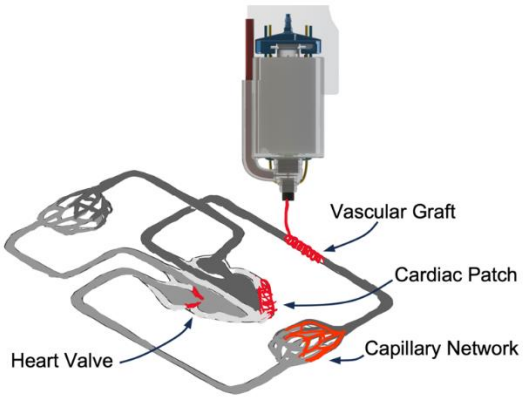

Figure 12: Table of content graphic: MEW scaffolds with tuned structure-function properties for the treatment of cardiovascular diseases.

Contribution statement of **Kilian M. A. Mueller**: conceptualization, data curation, investigation, methodology, visualization, writing – original draft, writing – review and editing.

8. Introducing Controlled Microporosity in Melt Electrowriting

Kilian M. A. Mueller, Andreas Unterrainer, Diana M. Rojas-González, Elena De-Juan-Pardo, Marian Willner, Julia Herzen, Petra Mela

Advanced Materials Technologies 8:6, 2023

Supporting materials associated with this article can be found in the online version at DOI: 10.1002/admt.202201158

Scaffolds produced via MEW are exploited for their tunable structure-property relationship. Yet, they are typically macroporous and, therefore, require the combination with another biomaterial or biofabrication process to obtain a microporous construct.

To date, the phenomenon of fiber bridging has limited the achievable pore size. Fiber bridging describes the effect that the fiber jet deviates from the planned deposition path when positioned closer to a previously deposited fiber then a threshold interfiber distance. Hence, electrostatic attraction between these fibers lead to bridging and, in turn, fiber fusion. This results in loss of control over the fiber architecture and, consequently, the mechanical properties.

Here, a design approach is proposed that results in microporous MEW fiber architectures without fiber bridging. To this end, sets of parallel fiber arrays are angularly shifted and stacked. Within the parallel fiber arrays each fiber is positioned at an interfiber distance larger than the fiber bridging threshold. Randomization of the starting point of each array and superposition of the arrays results in scaffolds with pore sizes far smaller the fiber bridging threshold. The resulting pore size can be controlled by adjusting the interfiber distance per array and/or by tuning the number and orientation of angular superpositions. Toolpaths for these microporous architectures are algorithmically generated via a MATLAB toolbox, which is easily accessible via a graphical user interface.

Furthermore, this approach allows to decouple fiber diameter from pore size as demonstrated via micro computed tomography. Here, scaffolds were produced via the identical Gcode but from fibers of different diameter (5.1 ± 0.7 µm to 21.8 ± 1.7 µm) and

yet they showed similar pore diameter distributions each peaking at 45 µm. This finding is in strong contrast to electrospinning, where pore size depends on fiber diameter.

Additionally, structural and, hence, mechanical anisotropy can be introduced in the scaffold architecture by using only selected angle shifts for the superimposed fiber arrays. In this way, an anisotropy ratio of up to 7.5 could be achieved, which matches that of aortic valve tissue.

Efficient cellular infiltration was found for scaffolds with a fiber diameter of 9.6 ± 0.7 µm and a pore size distribution peaking at approximately 45 µm. Here, human umbilical artery smooth muscle cells (HUASMCs) migrated cross the scaffolds' thickness and covered a cross-sectional scaffold area fraction of 10.9 ± 2.2 % after seven days of culture. After 28 days of culture extracellular matrix production was evident in the scaffold's micropores.

Ultimately, the design strategy was translated towards tubular architectures. This allowed the production of small diameter (Ø 4 mm) microporous scaffolds with a suture retention force of 1.2 ± 0.2 N and 2.6 ± 0.5 N for 150 µm and 300 µm wall thickness, respectively. Also, covered stents can be produced using this design methodology.

In conclusion, this work presents an efficient design strategy for the fabrication of flat and tubular microporous scaffolds with tunable mechanical properties. This obviates the need to combine MEW with other biofabrication techniques to obtain pores sizes adequate for e.g. cardiovascular *in situ* tissue engineering.

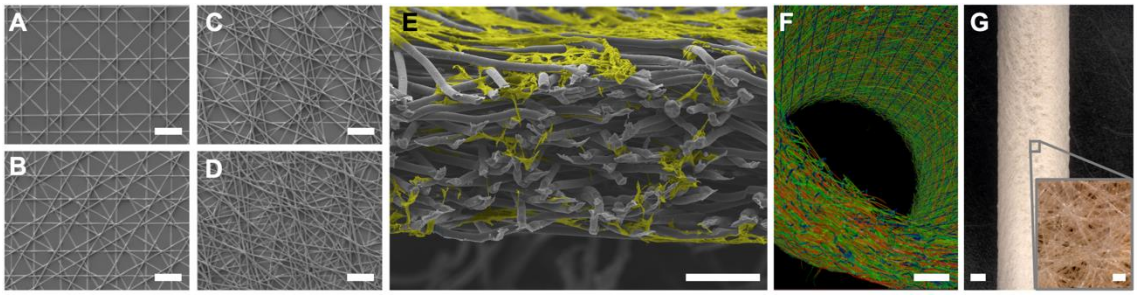

Figure 13: Table of content graphic: Microporous MEW scaffolds. A, B, C, D) Increasing numbers of angularly shifted superpositions of parallel fiber arrays decreased pore size (scale bars 200 µm). E) View into the scaffold's cross-section with cellular infiltration after seven days of culture (scale bar 100 µm). F) Reconstructed and color-coded (per orientation angle) microCT data of a tubular scaffold (scale bar 1 mm). G) Small-diameter vascular graft with microporous wall (scale bar 1mm, inset 100 µm).[63]

Contribution statement of **Kilian M. A. Mueller**: conceptualization, data curation, formal analysis, investigation, methodology, software, validation, visualization, writing – original draft, writing – review and editing.

9. Small-diameter Vascular Grafts with Tunable Compliance via Melt Electrowriting for In Situ Tissue Engineering

Kilian M. A. Mueller, Christina Ahrens, Linda Grefen, Salma Mansi, Dario Arcuti, Elena M. De-Juan-Pardo, Felix Kur, Christian Hagl, Petra Mela

Unpublished

Contribution statement of **Kilian M. A. Mueller**: conceptualization, data curation, formal analysis, investigation, methodology, software, validation, visualization, writing – original draft, writing – review and editing.

Abstract

In clinical practice, synthetic vascular grafts are advantageous due to their immediate availability but are burdened by high failure rates in small diameter settings because of thrombogenicity, infections, and intimal hyperplasia (IH). A mismatch in compliance between graft and host vessel has been identified as major contributor to the development of IH. Here, we propose a fabrication method to produce polymeric small-diameter vascular grafts with controlled compliance based on a spiral microfiber architecture via MEW. By realizing a microporous graft wall, we follow the paradigm of in situ tissue engineering with the promise of combining the advantages of synthetic (off-the-shelf) and autologous (living) grafts. Controlling the fiber winding angle enabled tunable compliances in the full physiological range of arteries and veins. Leveraging this, we introduced a gradient in the fiber architecture to achieve arteriovenous grafts matching the compliance of the target vessels at their ends (arterial vs. venous compliance) with a continuous smooth transitional region in between. The potential for clinical translation is demonstrated *in vitro* by meeting criteria for suture-retention, anti-kinking behavior, burst pressure, and self-sealing after cannulation.

9.1. Introduction

Autologous arteries or veins are the current gold standard for small-diameter vessel substitutes e.g. for coronary artery bypass grafting (CABG).[164] However, autografts are of limited availability, may be of unsuitable quality, and can cause donor site morbidity.[165,166] Therefore, synthetic grafts evolved as promising off-the-shelf alternative with immediate availability. Despite their satisfactory performance in large-diameter settings, synthetic grafts are plagued by low patency rates when used as small-diameter prostheses, mainly caused by surface thrombogenicity and the development of intimal hyperplasia (IH).[89]

Tissue engineering (TE) holds the potential of providing artificially produced living vessels to the patients.[167] Specifically, the paradigm of *in situ* TE synergizes the immediate availability of synthetic grafts with the long-term functionality of living autologous vessels.[103] *In situ* tissue-engineered grafts are initially cell-free scaffolds, and once implanted, exploit the innate regenerative potential to stimulate endogenous tissue formation while degrading.[84,168] Careful scaffold design is imperative, both from a biological and a mechanical perspective. In fact, a mismatch in compliance, that is the radial extensibility of a vessel in response to a luminal pressure wave, has been identified as a major contributing factor to IH.[169–171]

Indeed, studies showed that tissue-engineered vascular grafts (TEVGs) with the same compliance resulted in viable neotissue formation in the venous circulation, while they failed catastrophically when implanted in the arterial circulation of mice.[172] Similarly, identical grafts had higher occlusion rates when implanted in the carotid than in the abdominal aorta of rats.[173] These findings highlight the pressing need for grafts whose compliance can be specifically tailored to the target vessel. This can also be extrapolated to larger diameters such as the human ascending aorta where comparatively stiff Dacron grafts are often used, resulting in up- and downstream cardiovascular problems as reported in the clinical literature.[174]

MEW has emerged as a powerful biofabrication technique that offers unique control over biomimetic scaffold mechanics due to its targeted microfiber placement.[12,38] Assisted by an electric field, MEW stacks polymer microfibers along predefined pathways into multi-layered architectures resulting in precisely defined porous scaffolds.[12,38] This has been extensively exploited for cardiovascular TE,[175] e.g. for heart valves[44,66,70,90] and cardiac patches.[69,176–180] MEW is gaining increasing interest for TE of small-diameter vascular grafts (SDVGs),[60,63,85,86,91,181–186] but surprisingly only a minority of the work[86,183,185,186] investigated the resulting compliance, despite its crucial importance as fundamental

mechanical characteristic. Also, critical aspects for successful clinical translation such as anti-kinking behavior are to date only rudimentarily reported if not ignored in these reports.[86,184] Federici *et al.* described a graft based on a fixed polycaprolactone (PCL) MEW fiber architecture infused with a lyophilized fibrinogen matrix and covered by an additional solution electrospun layer of poly(L-lactide-co-ε-caprolactone) (PLCL).[86] This graft design required three different fabrication processes, including the use of toxic solvents for electrospinning, and, instead of taking advantage of the tunable structure-property relationship of MEW scaffolds, the compliance of the construct was tuned via the thickness of the electrospun outer layer, similarly to what previously shown by Fernández-Colino *et al.*, although for a polyvinylidene fluoride (PVDF) warp-knitted textile infiltrated with an elastin-like recombinamer and covered by a electrospun PCL layer.[187] Chen *et al*. used a dense MEW outer scaffold, which showed collapsed and fused fibers due to excessive heating, to prevent dilation of their inner MEW scaffold, yet they did not further leverage the MEW fiber architecture to tailor the resulting compliance.[186] Other reports on compliant MEW fiber patterns follow the *in vitro* TE approach, where the macropores of linear[183] or sinusoidal[185] fiber architectures were bridged by cells cultured for multiple days. Weekes *et al.* report two different compliance values for their sinusoidal architecture that were obtained by changing the fiber spacing (250 µm and 500 µm) of an otherwise identical fiber architecture.[185] Sinusoidal fiber architectures have already been shown to be interesting for MEW scaffolds to mimic the J-shaped stress-strain response of cardiovascular soft tissues.[44,66,90]

In contrast, we propose a tunable strategy for the fabrication of SDVGs with the capability to match the compliance of the native target vessel only by design of the MEW fiber architecture, over the entire anatomical range (venous to arterial compliance). We comply with the requirements of *in situ* TE not by adding an electrospun layer for microporosity, but instead exploiting a multiscale MEW scaffold embedded in a gelatine matrix, hence obviating the need for toxic solvents. These grafts show excellent handling and anti-kinking behavior and the grafts' design strategy offers the option of introducing a compliance gradient, e.g. for arteriovenous grafts (AVGs) where the implant is connecting an artery and a vein.

9.2. Results and Discussion

9.2.1. Fiber Winding Angle Tunes Compliance Characteristics

We hypothesized that controlling the winding angle of linear melt-electrowritten fibers along the graft's longitudinal axis allows to tune the compliance. Building on our

previously reported software platform for MEW constructs,[63] we generated fiber architectures for tubular scaffolds from multiple intertwined helices with fiber winding angles ranging from ± 15° to ± 75° (**Figure 14A, B**). These linear fiber paths were connected with circular segments at the ends of the grafts to result in a single uninterrupted toolpath as required by the continuous fiber deposition nature of MEW. The distance between parallel fibers was set to 750 ± 50 µm. This quasi-equidistant setting was dictated by the geometric restriction of keeping the graft's circumference constant for the different winding angles and with a constant number of helices per graft. These programmed fiber architectures were fabricated by precisely depositing polycaprolactone (PCL) microfibers onto 4 mm diameter cylindrical collectors. 15 layers of fibers with a diameter of 24.2 ± 1.6 µm were stacked.

In accordance with ISO 7198, the compliance of the constructs was determined by measuring the change in diameter in response to cyclic changes in the luminal pressure from 80 to 120 mmHg created by inflating a high-compliance silicone liner (25.7 ± 3.5 %(100 mmHg)$^{-1}$) inside the scaffold (**Figure 14C**). Here, we found compliances ranging from 12.7 ± 2.0 %(100 mmHg)$^{-1}$ for the ± 15° scaffolds down to 0.6 ± 0.4 %(100 mmHg)$^{-1}$ for scaffolds with ± 75° fiber winding angles (**Figure 14D**). This tunable structure-property relationship allows to cover the range of compliances of native human arteries (4.7 – 17.0 %(100 mmHg)$^{-1}$)[188–196] and veins (0.7 – 3.7 %(100 mmHg)$^{-1}$)[194–198] in contrast to the stiff clinically used synthetic grafts made of polytetrafluoroethylene (PTFE) (0.2 – 0.9 %(100 mmHg)$^{-1}$) or Dacron (0.8 – 1.9 %(100 mmHg)$^{-1}$).[195,196,199]

Controlling the winding angle of linear fibers, as shown here, is a simple, yet effective design strategy to tune the compliance of macroporous scaffolds. Additionally, the fiber spacing, i.e. the fiber density, can be used to fine-tune the compliance, with larger fiber spacings resulting in higher compliances as exemplarily shown for a ± 45° fiber winding angle (**Figure 14E**). This trend is in contrast to the work of Weekes *at al.*, who showed a higher compliance for sinusoidal fiber patterns when fiber spacing decreased from 500 µm to 250 µm.[185] The compliance could potentially be further adjusted by varying other MEW process parameters, such as the fiber diameter or the layer number.

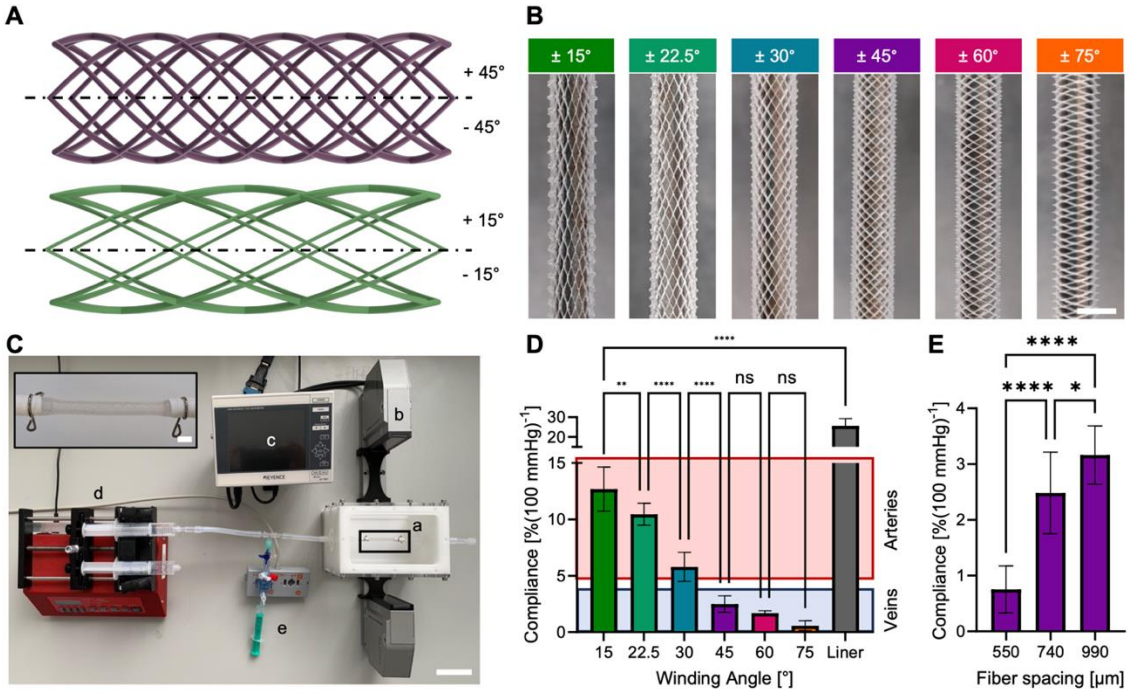

Figure 14: Fiber winding angle controls the compliance of melt-electrowritten tubular scaffolds. A) Schematic representation of tubular architectures with two complementary fiber winding angles (purple: ± 45°, green: ± 15°, fiber diameters not to scale). B) Macroporous MEW scaffolds with fiber winding angles ranging from ± 15° to ± 75° on 4 mm diameter collectors (scale bar 4 mm). C) The compliance was determined by a) mounting the scaffolds orthogonally to the light path of b) an optical micrometer. A c) control unit visualized the changes in scaffold diameter in response to varying luminal pressures applied via d) a programmable syringe pump and recorded via e) a pressure sensor (scale bar 5 cm, inset scale bar 4 mm). D) Compliance obtained with different fiber angles covered the range reported for human arteries (red shaded box) and veins (blue shaded box). E) Varying the interfiber distance while keeping the winding angle constant (here ± 45°) is an additional option for fine tuning the compliance.

9.2.2. Combining Macro- and Microporosity Forms Multiscale Scaffolds

Scaffolds for *in situ* TE require a microporosity to host cells for endogenous tissue formation.[168] Therefore, we combined the macroporous fiber pattern with a microporous matrix, which was melt-electrowritten in a first step to later form the graft's luminal side, following our approach to introduce microporosity for cell infiltration (**Figure 15A**).[63] To this end, we varied the MEW process parameters to obtain much smaller fibers with 9.2 ± 0.6 µm diameter and printed a fiber pattern based on the superposition of angularly shifted sets of parallel fibers (200 µm inter fiber distance) on 4 mm diameter collectors. These parallel fiber sets were shifted ± 5° and ± 15° relative to the main fiber winding angle of the macroporous fiber pattern (e.g. ± [30°, 40°, 50°, 60°] for a ± 45° macroporous pattern). Five stacks of the microporous pattern resulted in pore sizes of 7.9 ± 5 µm (**Figure 15B**). This pore size will not change if the main fiber winding angle is varied, but instead can be steered by changing the fiber spacing or the number of fiber sets.[63]

In a second step, we deposited the macroporous fiber pattern (as described in the section above) onto the microporous base matrix. This is the first graft fabrication strategy building only on MEW design parameters to generate a microporous vessel wall

with tunable compliance. An additional benefit of such strategy is that no solvents were used, as in contrast to previous studies, where MEW has been combined with solution electrospinning to provide microporosity and tune the grafts' compliance.[85,86,91] Also, this work presents a fabrication workflow where the graft is produced in a single MEW print job, instead of joining two separately produced tubular MEW components and relying on friction in between them as presented by Chen *et al*.[186]

Potentially, the MEW graft could be used as is, relying on hemostasis to seal the vessel wall as shown for electrospun vessel substitutes.[200,201] Alternatively, it could be complemented with a soft matrix, as long as it is not interfering with the compliance given by the MEW architecture. Here, we chose to add gelatine by dip-coating, which resulted in a total wall thickness of 1300 ± 100 µm (**Figure 15C**).

As verified for some of the fiber angles, the compliance of the composite grafts was well in agreement with that obtained for the macroporous architectures alone (**Figure 15D**). Because the fiber pattern for the microporous matrix is based on the same design principle as in the macroporous architecture, it did not suppress the deformation mechanisms of the macroporous patterns with fiber winding angles of ±15° and ±30°.

Gelatine is provides effective cell adhesion sites[202] and is considered to support the formation of endothelium.[203] Indeed, platelet adhesion and activation (**Figure 15E-G**) was significantly reduced on gelatine versus ePTFE and fibrin. We found hemolysis (**Figure 15H**) to be in the range of the reference materials or negative controls. Coagulation time of the gelatine matrix (**Figure 15I**) was slightly shorter than that of ePTFE but similar to the negative control. Hemocompatibility could further be improved by functionalizing the gelatine matrix with anticoagulants such as heparin.[204,205] Successful formation of an endothelial cell layer lining the lumen was found after 4 days of static culture of the tubular constructs (**Figure 15J**).

Upon implantation the grafts need to withstand the dynamic physiological pressure levels. Burst pressure was determined to be 1411 ± 280 mmHg, which is in the range of the human saphenous vein (1599 ± 877 mmHg),[193] but lower than that of the human internal mammary artery (3196 ± 1264 mmHg)[193] (**Figure 15K**). There is no minimal burst pressure defined by the ISO 7198.

Next, we quantified the suture retention force to be 0.7 ± 0.3 N (**Figure 15L**). Although this value is below those reported for the human saphenous vein (1.92 ± 0.02 N)[193] and internal mammary artery (1.35 ± 0.49 N),[193] suturing the grafts to a porcine right coronary artery (**Figure 15M**) and to human saphenous veins by an experienced cardiac surgeon was unproblematic. The anastomosis to the coronary artery performed in the

end-to-side fashion as it would be done for a coronary artery bypass graft (CABG). Our tubular scaffolds could be handled conveniently and could be cut to the required length at any graft position without losing total integrity as the individual PCL fibers fused at their crossing points.

In contrast, Federici *et al.* had to use a stiff connection device to anastomose their graft (fixed MEW fiber pattern covered by electrospun layer) to a rat abdominal aorta as securing the graft via the eversion method had failed.[86] While we used a running suture, it is evident that the suture style affects anastomotic compliance.[206] In this context, it could be beneficial to apply degradable suture materials or suture-less approaches, such as glueing, to avoid jeopardizing the anastomotic compliance.[207,208]

It is crucial to prevent kinking of vascular prostheses, for example when implanted in a loop configuration for vascular access or as interposition graft in a vessel along a bending joint. ISO 7198 suggests a reduction of 50 % of the luminal diameter as threshold for kinking. Here, we found no reductions of the grafts' outer diameter larger than 50 % even for bending radii as low as 1.5 mm (**Figure 15N**). Under the assumption of an incompressible wall thickness, kinking, therefore, did not occur. This excellent anti-kinking behavior inherently originates from the intertwined multi-helix design of the microfiber MEW architecture. Similarly, although at a much larger scale, Wu *et al.* identified a single spiral pattern to be the optimum anti-kinking reinforcement pattern, that was printed onto electrospun grafts via fused filament fabrication.[209] However, the effect of such reinforcement on compliance was not evaluated.

Although here demonstrated with gelatine for tissue engineering application, the MEW matrix could be embedded in a non-degradable polymer, e.g. silicones or thermoplastic polyurethanes, to achieve a 'classical' prosthesis as alternative to the clinically available ones.

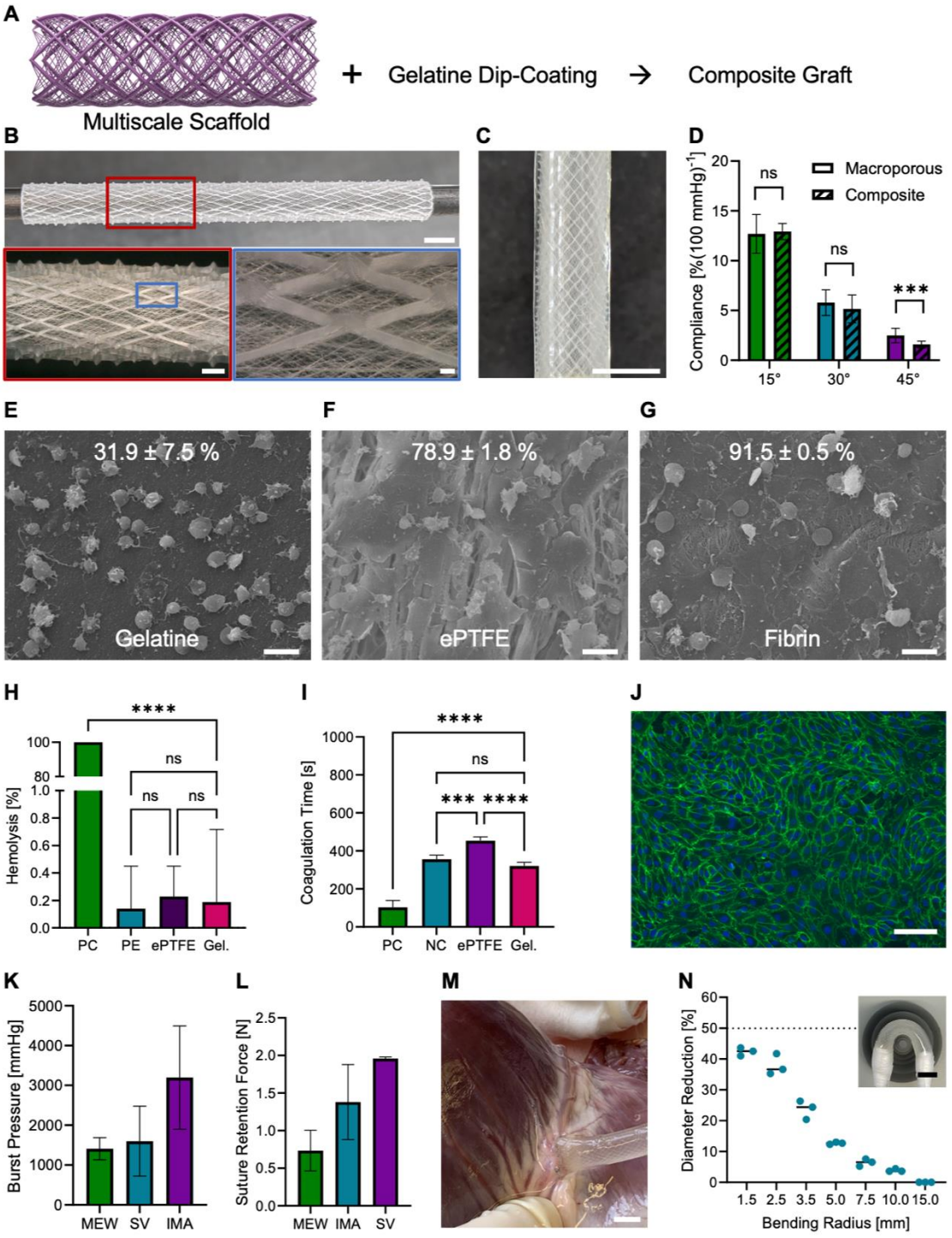

Figure 15: Compliant tubular scaffolds via MEW. A) Schematic representation of the design concept: combining an inner microporous MEW matrix with an outer macroporous MEW fiber architecture resulted in multiscale scaffolds. B) Scaffold on a 4 mm diameter mandrel highlighting accurate fiber stacking of the macroporous architecture (scale bars 4 mm, 1 mm, 100 µm). C) Scaffold after dip-coating in gelatine (scale bar 4 mm). D) The composite scaffolds showed compliances similar to those obtained for the macroporous scaffolds alone. E) Platelet adhesion and activation on gelatine was lower than for F) the ePTFE reference material, while G) fibrin showed a strong activation potential. Area coverage by platelets per material (scale bars 5 µm). H) The hemolysis induced by the gelatine matrix (Gel.) was comparable to polyethylene (PE) and expanded polytetrafluoroethylene (ePTFE) (positive control (PC): whole blood diluted in water). I) The coagulation time for contact with gelatine was found to be significantly longer than for the PC (fibrin) and similar to negative control (NC: citrated platelet poor plasma) and ePTFE. J) The luminal surface of the graft supported endothelial layer formation in static conditions (scale bar 100 µm). K) Burst pressures were comparable to that of the human saphenous vein (SV) but lower than that of the human internal mammary artery (IMA). Values for SV and IMA taken from Konig *et al*.[193] L) Suture retention force was lower than that of human IMA and SV. Values for SV taken from L'Heureux *et al*.[197] and for IMA taken from Konig *et al*.[193]

M) However, anastomosing to a porcine right coronary artery was unproblematic. The coronary artery was successfully pressurized via the graft (scale bar 4 mm). N) No diameter reductions of more than 50 % were observed, even for bending radii as low as 1.5 mm, indicating anti-kinking behavior. Inset is showing bending of a graft around a 3.5 mm radius template (scale bar 10 mm).

9.2.3. Fiber Architectures for Compliance Gradient in Arteriovenous Grafts

Patients with end stage renal disease rely on functional vascular access (VA) to receive successful hemodialysis. As first option for VA, international guidelines propose the creation of an autogenous arteriovenous fistula (AVF).[210,211] However, AVFs are plagued *inter alia* with long maturation times of several months[212] and high primary failure rates, particularly in the elderly.[213] Consequently and in light of a more patient-centered approach to VA, the “fistula first” strategy has been challenged.[214–216]

Alternatively, VA can be accomplished via arteriovenous grafts (AVGs), where a prosthetic conduit is surgically interpositioned between an artery and a vein, two distinctly different vessels in terms of compliance, and usually placed in the patient’s non-dominant forearm (**Figure 16A**). Using synthetic AVGs circumvents the problematic maturation time and performs well in short term.[169] However, synthetic AVGs are prone to develop neointimal hyperplasia typically at the vein anastomosis, potentially leading to stenotic failure.[169–171,217,218]

We introduced a spatially heterogenous fiber architecture to obtain a compliance gradient in the resulting grafts to mediate between venous and arterial compliance while matching the compliance at the anastomosis sites. This graft design consists of three regions: i) arterial compliance, ii) venous compliance, and iii) a gradient region to provide a mechanically smooth transition between region i) and ii). The gradient region was obtained by designing a fiber path along a cubic spline that tangentially connects the linear fibers at the grafts ends where either a venous or arterial compliance prevails (**Figure 16B, C**). This gradient approach was translated to both the microporous and the macroporous fiber architecture (**Figure 16D**). To maintain the graft’s diameter constant along the length, in the region with the larger fiber angle (venous region with lower compliance) the distance between parallel fibers will be decreased. This geometric restriction is beneficial for the compliance gradient, since the slight difference in fiber density only further supports the compliance difference between venous and arterial regions.

A luminal pressure of 120 mmHg resulted in different graft diameters at the arterial and venous side with a smooth transition in diameter along the graft’s central region (**Figure 16D**), reflecting the compliance gradient.

The grafts were then sutured to human saphenous veins and porcine femoral arteries in end-to-end style. In both cases the grafts pulsated at the anastomoses with the same amplitude as the corresponding native vessels when subjected to pulsatile flow (**Figure 16E, F**).

Furthermore, the grafts were successfully cannulated using an 18 G needle while being pressurized to 120 mmHg. After retracting the needle, the graft was self-sealing (**Figure 16G**). Once implanted this will be further supported by hemostatic effects and tissue healing.

For the first time, this work presents a gradient tubular scaffold architecture via MEW to enable a smooth transition of mechanical properties between two distinctly different regions. So far, MEW scaffolds with spatially heterogenous patterns have been shown in-plane[44,65,219] and across the scaffolds' thickness.[26,186,220–222] However, they were strictly separated in regions with discrete mechanical properties and a transitional region was missing. Although demonstrated for flat scaffolds in the context of MEW scaffolds for heart valves, Vernon *et al.* advocated for the importance of engineering interfaces between regions as these are potential regions for onset of mechanical failure and pointed to the superior performance of continuous fiber interfaces as compared to overlapping or suture-like interfaces.[70] Here, we obsolete this by replacing interfaces between distinctly different regions with a smooth gradient transitional pattern.

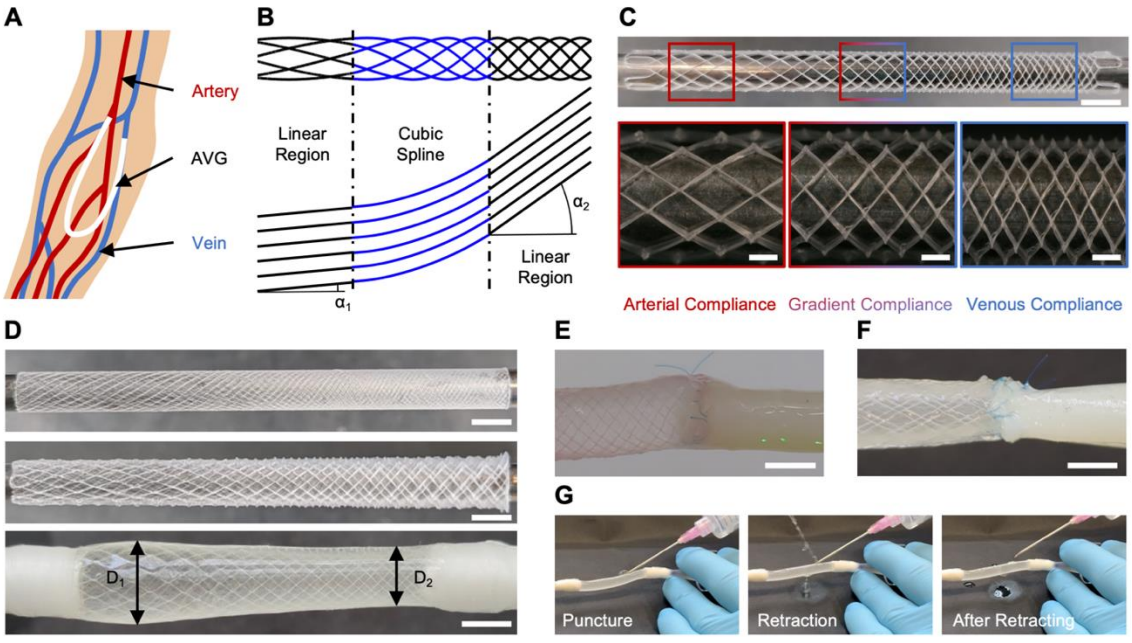

Figure 16: Gradient-compliance scaffolds for arteriovenous grafts. A) AVGs connect an artery and a vein, usually in a loop configuration in the forearm. B) To accommodate the two distinct compliances (artery vs. vein) at the ends, the grafts feature a central gradient region. The schematic demonstrates the connection of the terminal linear fiber patterns (α_1 vs. α_1) by a cubic spline to result in a continuous fiber path for MEW. C) Melt-electrowritten macroporous gradient scaffolds with magnified images highlighting the different fiber patterns within the same graft (scale bars 4 mm, 1 mm). D) The gradient fiber architecture was translated to

the microporous matrix as well. The composite grafts showed gradient compliances manifested by diameters varying along the axial direction despite a constant luminal pressure (scale bars 4 mm). E) Vascular graft anastomosed to a human saphenous vein and F) porcine femoral artery (scale bars 4 mm). G) After cannulation with an 18 G needle the grafts were leak-free.

9.3. Conclusion

This work introduced compliant small-diameter vascular grafts, based on an intertwined multi-helix arrangement of polymeric microfibers fabricated via MEW. Leveraging the tunable structure-property relationship of MEW fiber architectures by controlling the winding angle, we realize grafts with compliance matching the range reported for human vessels from veins to arteries. This holds the potential of avoiding a compliance mismatch, which has been identified as major driver for implant failure. Building on that approach, we introduced a gradient architecture to obtain tailored grafts with gradually transitioning compliance from arterial to venous values along their length. This could be of particular benefit for *in situ* tissue-engineered arteriovenous grafts. By combining excellent handling and anti-kinking behavior with adequate suture retention force, burst strength, and hemocompatibility, this technology platform provides promising aspects for clinical translation.

9.4. Experimental Section

Gcode Generator

Our previously reported software platform based on MATLAB R2020b (The Mathworks, USA) outputs Gcode commands tailored to MEW of super positioned, angularly shifted sets of parallel fiber lines.[63] Here, this platform was upgraded combining two regions of different linear fiber architectures via the integration of cubic splines to result in gradient spatially heterogenous fiber pattern.

Melt Electrowriting

MEW was performed on an-inhouse developed setup. Briefly, the system consisted of two linear mechanical-bearing screw-driven stages (PRO115SL, Aerotech, Germany) for the X and Z direction and a direct-drive rotary stage (ADRS100, Aerotech, Germany) for rotation in the Y direction (circumferential direction of the grafts) that were controlled by Automation1 Studio (Aerotech, Germany). The MEW print head was mounted on the Z-axis and was designed to host a syringe (3cc Optimum, Nordson EFD, USA) equipped with a 23 G needle (Nordson EFD, USA) protruding about 1 mm from the print head. Both the syringe and the needle were individually heated via a temperature control unit (MIUE04003F/MIUE06012D and MI8844820G, Hotset, Germany). Polymer extrusion

was driven by pressurized air applied to the syringe via an electro-pneumatic controller (ITV1050-31F1CL3, SMC, Japan) and fiber formation was initiated by applying a positive electrical potential (MPL 200-30000 POS, FuG Elektronik, Germany) to the needle while the cylindrical metal collector (4 mm diameter) was electrically grounded.

Medical grade poly(ε-caprolactone) (Purasorb PC12, Lot# 2004002576, Corbion, Netherlands) was melted at 75 °C in the syringe and extruded via the needle at 85 °C. MEW was performed at a working distance of 4.0 mm between the print head and the collector with a voltage of 5.6 kV, print speed of 210 mm min^{-1}, and air pressure of 2 bar for the macroporous patterns and 5.3 kV, 440 mm min^{-1}, and 0.5 bar for the microporous patterns.

Composite Grafts

The multiscale scaffolds were composed of a melt-electrowritten microporous fiber matrix and a macroporous fiber architecture, both embedded in gelatine. The microporous pattern had five stacks of parallel fiber sets (200 µm inter fiber distance) shifted ± 5° and ± 15° relative to the main fiber winding angle of the macroporous fiber pattern (e.g. ± [30°, 40°, 50°, 60°] for a ± 45° macroporous pattern). The macroporous pattern consisted of 15 layers of intertwined helices with 750 ± 50 µm inter fiber distance. For dip-coating 5 g type A gelatine from porcine skin (Sigma Aldrich, USA) was dissolved in 50 ml deionized water under constant stirring (60 min, 400 rpm) at 60 °C. Separately, 350 µg transglutaminase (BDF Natural Ingredients, Spain) was dissolved in 1 ml deionized water. The transglutaminase solution was added to the gelatine solution at a ratio of 1:100. Heating was stopped and once the gelatine solution reached 35 °C, the MEW scaffolds, still sitting on the collector, were dip-coated. To ensure consistent gelatine thickness, the scaffolds were kept rotating while cooling down to room temperature.

Compliance

Compliance (n = 3, i = 4) was measured in accordance with ISO 7198. Here, the scaffolds were mounted into a measurement chamber orthogonally to the light path of an optical micrometer (LS-7030(M), Keyence, Germany). The scaffolds were closed on one outlet side of the measurement chamber, while via the other side pressure was applied using a programmable syringe pump (LA120, Harvard Apparatus, USA) and monitored via a pressure sensor (Xtrans, Codan Medizinische Geräte, Germany). For the macroporous scaffolds only, a silicone liner was inserted into the lumen in agreement with ISO 7198. The compliance of the silicone liner was 25.7 ± 3.5 %$(100\ mmHg)^{-1}$.

While applying a pulsatile pressure profile (80 to 120 mmHg, 60 ± 10 pulses per minute) to the graft, changes in its diameter were recorded by the optical micrometer. A python script collected all data and calculated the dynamic compliance according to ISO 7198:

$$C = \frac{(r_{p_2} - r_{p_1})/r_{p_1}}{(p_2 - p_1)} \times 10^4$$

where p_1 is the lower internal pressure and r_{p_1} the corresponding radius and p_2 is the higher internal pressure and r_{p_2} the corresponding radius.

Suture Retention

Suture retention was determined following ISO 7198 by inserting a 7-0 polypropylene suture (Covidien Surgipro II VP-704-MX, Medtronic, Ireland) approximately 2 mm from the graft's end and mounting the suture to the moving clamp of a tensile testing machine (Zwickline Z2.5, 10 N load cell, ZwickRoell, Germany). The opposite side of the graft was immobilized in the other clamp of the tensile testing machine. The measurement was performed at a cross-head speed of 50 mm min^{-1}. Composite grafts with 45° (n = 4) and 15° (n = 3) fiber pattern were tested. Grafts were also sutured to human saphenous veins, porcine right coronary arteries, and porcine femoral arteries via a running suture (8-0 polypropylene, Prolene, Ethicon, USA).

Burst Pressure

Burst pressure (n = 5) was assessed according to ISO 7198. A planar sample (1 cm x 1 cm) was excised from composite grafts with a 45° fiber pattern and placed inside a testing chamber, featuring a 4 mm diameter hole against which the samples were pressed by applying pressure via a syringe. Pressure was recorded via a pressure sensor (MIDAS 401001/000, Jumo, Germany) and the peak pressure at failure was recorded as burst pressure.

Kinking Radius

To evaluate the kinking behavior, composite grafts (n = 3, ±30° main fiber winding angle) were pressurized with 100 mmHg and bent around a template featuring radii from 1.5 mm to 15 mm. The reduction in diameter was quantified via:

$$\Delta D = 100\% \times \frac{(D_0 - D_1)}{D_0}$$

where D_0 is the graft's diameter in relaxed configuration and D_1 is the graft's diameter while undergoing bending.

Cannulation

Grafts were pressurized with a pulsatile pressure profile (80 - 120 mmHg, 1 Hz) and punctured with an 18 G needle (L1 0103, servoprax, Germany) at a 45° angle with respect to the longitudinal graft axis and the needle cut facing upwards.

Hemolysis

200 µl whole blood was diluted in 10 ml 0.9 % saline solution. The samples (n = 5, ~ 210 mm^2 surface area, high density PE (Raumedic, Germany) and ePTFE (GORE-TEX Cardiovascular Patch, W. L. Gore & Associates, USA) as reference materials) were incubated in 700 µl diluted blood under gentle agitation at 37 °C for 2 h. Whole blood incubated with distilled water or saline solution, served as positive control (PC) and negative control (NC) respectively. After centrifugation, the absorbance values of the supernatants were measured at 545 nm with a spectrophotometer (Spark, Tecan, Switzerland). Hemolysis rate was calculated using the following formula according to ASTM F 756:[223]

$$\%\, Hemolysis\ = \frac{Absorbance\ of\ test\ sample - Absorbance\ of\ NC}{Absorbance\ of\ PC - Absorbance\ of\ NC} \times 100$$

Coagulation Time

To assess the plasma recalcification time, the samples (n = 5, discs with 12 mm diameter) were incubated with 250 µl platelet-poor plasma (PPP) derived from citrated whole blood at 37 °C for 20 min. Fibrin (prepared by mixing fibrinogen and thrombin as reported previously)[224] served as PC, while PPP was used as NC, and ePTFE (GORE-TEX Cardiovascular Patch, W. L. Gore & Associates, USA) as reference. Upon addition of 100 µl $CaCl_2$ to 100 µl of each sample, the absorbance was measured with a spectrophotometer (Spark, Tecan, Switzerland) at 405 nm in 20 s intervals for 2 h to assess the time required to obtain a 5 % increase in fibrin formation as compared to the total increase.

Platelet Adhesion

600 µl platelet-rich plasma (PRP) was added to the samples (n = 3, fibrin[224] and ePTFE (GORE-TEX Cardiovascular Patch, W. L. Gore & Associates, USA) as controls) and incubated at 37 °C for 1 h. The samples were washed in PBS and fixated with 2 % glutaraldehyde prepared in PHEM buffer. They were then dehydrated by a series of increasing concentrations of ethanol (30, 50, 70, and 3 x 100 %) each for 15 min at room temperature and subsequent critical point drying (BAL-TEC GmbH, Germany). The samples were sputter coated (7 nm gold layer) and imaged using scanning electron

microscopy (accelerating voltage 10 kV, JSM-6390, Jeol, Germany) and the surface area covered by platelets was assessed using Fiji[225] plugins in ImageJ.[226]

Endothelialization

For the static endothelialization assessment, human umbilical vein endothelial cells (HUVEC) were used. The cells were cultured in endothelial cell basal medium (EBM-2, Lonza Group AG, Basel, Switzerland) supplemented with the endothelial growth medium 2 kit. Supplements included 0.1% ascorbic acid, 0.4% human fibroblast growth factor, 0.1% insulin, 0.1% gentamicin, 2% fetal bovine serum (FBS), 0.1% endothelial growth factor, 0.04% hydrocortisone, 0.1% epidermal growth factor and 0.1% heparin. The polymer scaffold was washed for 30 minutes using 70% ethanol and 30 minutes using sterile phosphate-buffered saline solution (PBS). It was then dip-coated in sterily prepared gelatine, and after complete crosslinking, it was positioned in sterile silicone tubing. The cells were seeded on the lumen of the tubular graft at a density of 50.000 cells/cm^2. The graft was clamped shut on both ends and incubated at 37 °C for six hours. Every 30 minutes, the graft was rotated 90° around its axis to ensure even distribution of the cells on the lumen. The graft was then removed from the silicone tubing, and prepared for immunostaining. The samples were fixed in 4% paraformaldehyde (Carl Roth, Germany) at room temperature for 15 minutes and washed in PBS 3 times each for 5 minutes. Blocking was performed in 5 % normal goat serum solution (DAKO GmbH, Jena, Germany) for 1 h at room temperature. Samples were incubated with the mouse anti-human primary antibody CD31 (Sigma, Germany) for 1 h at room temperature. After 3 washes in PBS for 5 minutes each, the graft was incubated in Alexa A488 seconday antibody for 1 h at room temperature. The samples were washed 3 times for 5 min in PBS and counterstained with DAPI nuclei acid stain (Carl Roth, Germany). The graft was carefully cut open along the longitudinal axis and images were taken with fluorescence microscope BZ-X800 (Keyence Corporation, Japan).

Microscopy and Image Analysis

Scaffolds were imaged using a digital light microscope (VHX-5000, Keyence, Germany) and fiber diameter (n = 4, i =3) was determined via the built-in software of the microscope. Pore sizes were evaluated using light microscopy images. Circles were automatically fitted into the pores (n = 3, i = 100) using an in-house developed MATLAB script. The diameter of the fitted circles was used to derive an average pore diameter.

Ethical Approval

Leftover anonymized human vein segments were obtained from CABG surgery performed at the Department of Cardiac Surgery at Ludwig-Maximilian University

Munich. Tissue was solely used if the patient's informed consent was given beforehand. This procedure was approved by the ethics committee of Ludwig-Maximilian University Munich (259-15). Porcine tissue was sourced from a local abattoir. Human blood was collected from informed donors following approval by the ethics committee of the Technical University of Munich (2023-40-S-SR). Human umbilical vein endothelial cells were collected and used in accordance with approval by the ethics committee of the Technical University of Munich (2023-531-S-KH).

Statistics

Statistical analysis was performed with Prism 9.2.0 (GraphPad Software, USA). After confirmation of normal distribution ANOVA, with post hoc Tukey multiple comparisons was performed. Values are reported as mean ± standard deviation. ****: $p \leq 0.0001$, ***: $0.0001 < p \leq 0.001$, **: $0.001 < p \leq 0.01$, and *: $0.01 < p \leq 0.05$ were used to indicate the level of significance.

10. Visualization of USPIO-labeled Melt-electrowritten Scaffolds by Non-invasive Magnetic Resonance Imaging

Kilian M. A. Mueller, Geoffrey J. Topping, Sebastian P. Schwaminger, Yunzhe Zou, Diana M. Rojas-González, Elena M. De-Juan-Pardo, Sonja Berensmeier, Franz Schilling, Petra Mela

Biomaterials Science 9:13, 2021

Supporting materials associated with this article can be found in the online version at DOI: 10.1039/D1BM00461A

To facilitate clinical translation of melt-electrowritten scaffolds, options for longitudinal monitoring via a clinically accepted imaging modality are required to enable follow up of the implant and informed decision making before eventual further interventions. MRI is a clinically validated non-invasive imaging technique. However, polymers such as those processed via MEW show limited image contrast in MRI due to their low proton density. It is clinical routine to employ contrast agents to increase image quality in MRI. However, this concept has not yet been transferred to melt-electrowritten scaffolds.

To this end, ultrasmall superparamagnetic iron oxide (USPIO) nanoparticles were chosen as contrast agents for MRI and incorporated into polycaprolactone (PCL). PCL was dissolved in acetone, up to 0.3 % w/w USPIOs were added, and the slurry was mixed in a sonication bath for 4 h to obtain a homogeneous particle distribution. Next, the resulting solutions were directly poured into the syringes for MEW and placed at room temperature for 48 h to let the acetone evaporate. The absence of any acetone residues was confirmed via Raman spectroscopy. The PCL color changed from white to brown with increasing USPIO concentration.

All composites were successfully melt-electrowritten into highly ordered wavy scaffold architectures onto a flat collector. No fiber instabilities such as fiber pulsing events were observed and all fibers showed a smooth surface as verified via SEM. Furthermore, straight fiber stacks of 40 layers were fabricated and tensile tested. Concentrations up to 0.2 % w/w UPSIOs caused small to no decrease in Young’s modulus and ultimate

tensile strength compared to pure PCL. Cytocompatibility was verified in a direct test with human umbilical artery smooth muscle cells (HUASMCs) following ISO 10993-5 for all composite concentrations.

For MRI the scaffolds were embedded into a 1 % w/w agar-agar hydrogel to assess their visibility in a 7 T preclinical MRI scanner within surrounding material. Pure PCL scaffolds were visible in nominally T1-weighted images, but showed no contrast with agar-agar in R1, R2, or R2* relaxation rate maps. On the contrary, increasing USPIO concentrations resulted in localized increases in contrast in R2 maps and strong effects on contrast in R2* maps.

This work demonstrates the potential of PCL-USPIO composites to improve visualization of melt-electrowritten scaffolds via the clinically accepted imaging modality MRI.

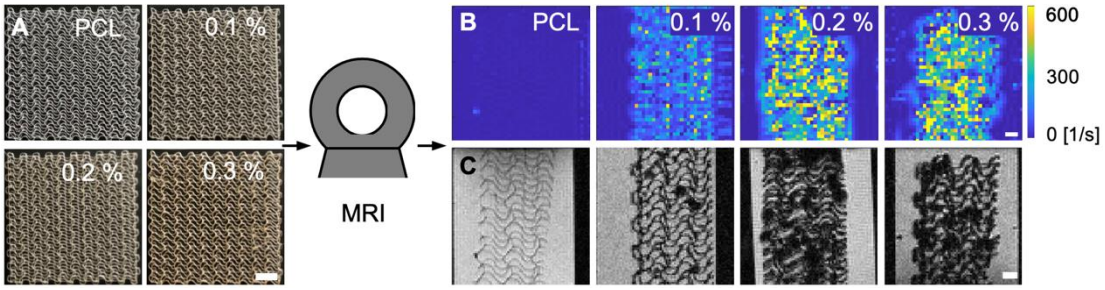

Figure 17: Table of content graphic: MRI visualization of MEW scaffolds. A) USPIO-labeling induced a color shift from white (pure PCL) to dark brown (PCL with 0.3 % w/w USPIO) (scale bars 4 mm) and enabled MRI visualization of MEW scaffolds by providing a strong contrast in B) R2* maps and in C) nominally T1-weighted images (scale bars 1 mm).[227]

Contribution statement of **Kilian M. A. Mueller**: conceptualization, data curation, formal analysis, investigation, methodology, software, validation, visualization, writing – original draft, writing – review and editing.

11. General Discussion and Conclusions

By outlining the development of various print head designs, a multi-axis kinematic platform, and software tools as well as by introducing new biomaterials to the MEW material library, this thesis advanced important technological aspects of MEW in general, while specifically targeting cardiovascular applications. The contributions to the MEW fields are indicated in **Figure 18** with respect to the generalized AM process chain:[228] i) a new material (PDO) and material composite (PCL+USPIO) was introduced, ii) a universal graphical Gcode generator was presented, and iii) filament-based MEW (F-MEW) and 5-axis MEW brought MEW to the next level and made it available to a large community. This together enables to produce cardiovascular scaffolds, that are anatomically correct, mechanically functional, and allow for longitudinal monitoring via magnetic resonance imaging.

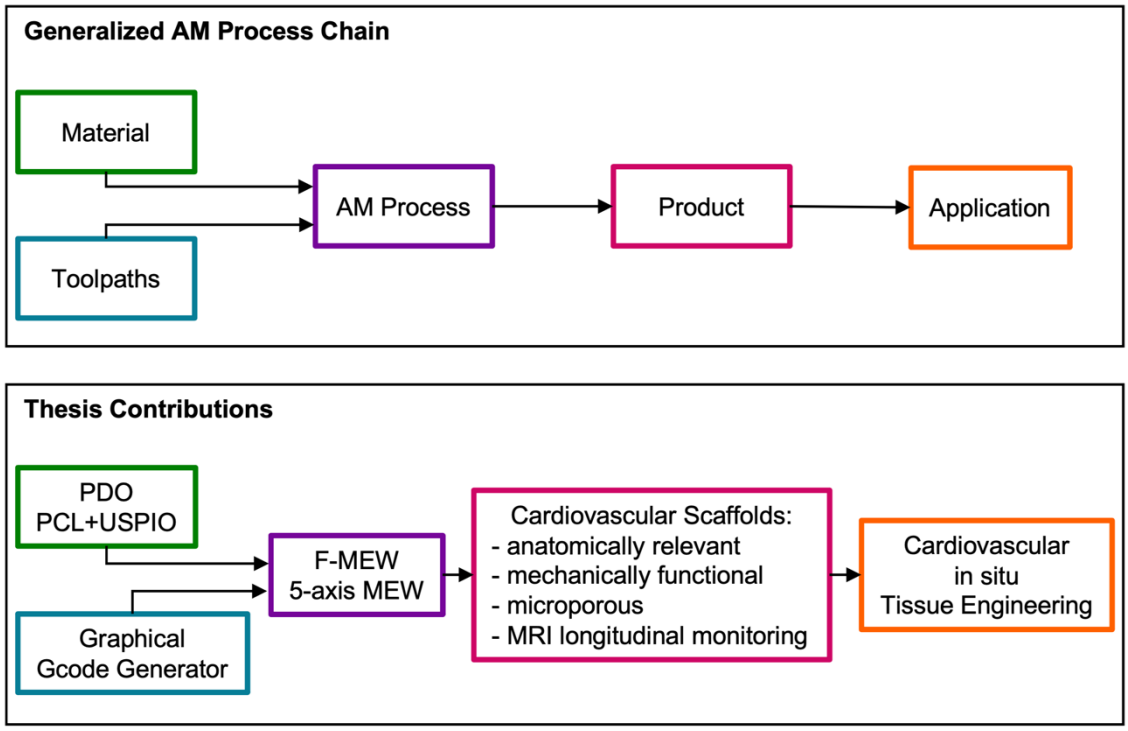

Figure 18: Contributions of this thesis to the different steps of the generalized AM process chain.

Introducing filament-based MEW allowed to exploit a melt-on-demand approach to reduce the thermal stress to thermosensitive polymers while simultaneously increasing accessibility of MEW by building on established machine components from the FFF ecosystem. However, introducing further polymers to the MEW material library will stay a multifaceted challenge as a plurality of requirements are posed upon these materials, such as compatibility of the material's melt temperature with the print head's maximum

operating temperature, suitable melt viscosity, adequate dielectric properties, and cytocompatibility.[99] Particularly, clinically used high-performance polymers, such as those from the polyaryletherketone (PAEK) family,[229] with a melt temperature of 300 °C and higher remain to be explored via MEW. While processing polymer melts is captivating for biofabrication applications due to a workflow without potentially toxic solvents, liquefying materials via a solvent route might be an option to significantly widen the material spectrum. Additionally, unlocking multimaterial MEW holds the potential of substantially improving the value of melt-electrowritten constructs by synergistically combining multiple material properties within a single construct. However, this will require the development of correspondingly complex MEW systems. Yet again, inspiration can be taken from the FFF ecosystem, where multi-nozzle print heads exist or, alternatively, the motion of two print heads is coordinated via a shared shuttle module.[230] Developing such a MEW system should ideally go hand-in-hand with integrating other biofabrication techniques, such as droplet- or extrusion-based bioprinting of (cell-laden) hydrogels, to hybridize advanced technologies with a better chance of mimicking the complexity of living tissues.[231]

Realizing the geometrical complexity of anatomically relevant MEW scaffolds was enabled via a 5-axis MEW platform. By building on an open-source project, this is a highly accessible and cost-effective approach. However, as reported, the electric field reorients the fiber jet perpendicularly to the collector's surface even if the needle is not always positioned orthogonally to the collector surface. Exploiting this phenomenon potentially enables to omit the fifth axis, hence opening avenues towards printing with four axes only. It remains to be explored for which use cases 4- versus 5-axis MEW will be superior. It is likely that 4-axis MEW will show inferior fiber deposition accuracy for collector geometries with surface elements that are parallel to the needle axis, as this will require an electric field-driven 90° reorientation of the fiber jet.

To demonstrate the achievable design complexity near-net-shaped reinforcement patterns for trileaflet valves were chosen as example for printing in 5-axis mode. However, these structures were not integrated into a tubular construct replicating e.g. the aortic root to form a valved conduit. Notably, *in situ* tissue-engineered valved conduits fabricated by fiber-forming techniques other than MEW have proceeded to large animal pre-clinical investigations (composite of jet-sprayed matrix with knitted support)[232] and clinical studies (valved conduits fabricated via solution electrospinning).[233,234] Yet, to date such a construct has not been fabricated via MEW. While a previous study had reported the fabrication of aortic root scaffolds including the sinuses of Valsalva via MEW,[52] combining this with leaflet structures inside will potentially require a modular collector for a sequential MEW process, where in a first step the leaflet architecture is

fabricated as presented in this thesis, followed by fabrication of the conduit by integrating the leaflet collector into additional cylinder-like collector components. Translating the gradient compliance approach to such a valved conduit might be of particular interest to facilitate the transition of mechanical properties from the stiff aortic annulus towards the compliant ascending aorta with its Windkessel effect.[235,236]

Complex print jobs require sophisticated toolpath planning. To avoid time-intense and error-prone manual preparation of Gcode, this can be accelerated via dedicated software platforms that generate toolpath commands either based on numeric user input values or by following a graphical approach, where the user virtually sketches the fiber paths onto a representation of the collector. Both approaches were demonstrated in this thesis. While particularly the graphical approach enables users without prior experience to generate Gcode even for highly complex print jobs, this will reach its limits when it comes to large fiber architectures which will require extensive sketching efforts. Here, algorithmically driven software packages, similar to slicing software for FFF, that automatically derive toolpaths starting from a virtual model of the part to be printed are urgently needed. By taking the process peculiarities of MEW into account, this can avoid that toolpath planning for large and complex constructs becomes a bottleneck for the future development of MEW.

Bringing tissue-engineered implants based on MEW scaffolds to a level, where clinical translation is within reach, requires efforts from multiple perspectives. This thesis focused mostly on technical aspects that were validated using PCL due to its excellent processability via MEW. However, PCL might not necessarily be the ideal material for cardiovascular applications as, while degrading, acidic byproducts cause local pH shifts, although somewhat mediated due to PCL's slow degradation rate.[97,98,237] Furthermore, the slow degradation of PCL, is not optimal, as timely degradation has been shown to be essential for rapid host remodeling of vascular grafts.[238]

In conclusion, this thesis has advanced the technological level of MEW to a potency that warrants further research towards *in vivo* studies and potentially clinical translation of MEW products.

References

[1] International Organization for Standardization, **2018**, ISO 52900.

[2] International Organization for Standardization, **2015**, ISO 17296.

[3] S. C. Altıparmak, V. A. Yardley, Z. Shi, J. Lin, *J. Manuf. Process.* **2022**, *83*, 607.

[4] R. Jones, P. Haufe, E. Sells, P. Iravani, V. Olliver, C. Palmer, A. Bowyer, *Robotica* **2011**, *29*, 177.

[5] B. N. Turner, R. Strong, S. A. Gold, *Rapid Prototyp. J.* **2014**, *20*, 192.

[6] T. D. Brown, P. D. Dalton, D. W. Hutmacher, *Adv. Mater.* **2011**, *23*, 5651.

[7] G. I. Taylor, *Proc. R. Soc. London. A. Math. Phys. Sci.* **1969**, *313*, 453.

[8] M. Yu, K. H. Ahn, S. J. Lee, *Mater. Des.* **2016**, *89*, 109.

[9] F. M. Wunner, M. Wille, T. G. Noonan, O. Bas, P. D. Dalton, E. M. De-Juan-Pardo, D. W. Hutmacher, *Adv. Mater.* **2018**, *30*, 1706570.

[10] Á. G. Marín, D. Lohse, *Phys. Fluids* **2010**, *22*.

[11] A. F. Spivak, Y. A. Dzenis, *Appl. Phys. Lett.* **1998**, *73*, 3067.

[12] T. M. Robinson, D. W. Hutmacher, P. D. Dalton, *Adv. Funct. Mater.* **2019**, *29*, 1904664.

[13] F. M. Wunner, P. Mieszczanek, O. Bas, S. Eggert, J. Maartens, P. D. Dalton, E. M. De-Juan-Pardo, D. W. Hutmacher, *Biofabrication* **2019**, *11*, 25004.

[14] K. L. O'Neill, P. D. Dalton, *Small Methods* **2023**, 2201589.

[15] G. Hochleitner, A. Youssef, A. Hrynevich, J. N. Haigh, T. Jungst, J. Groll, P. D. Dalton, *BioNanoMaterials* **2016**, *17*, 159.

[16] N. C. Paxton, J. Ren, M. J. Ainsworth, A. K. Solanki, J. R. Jones, M. C. Allenby, M. M. Stevens, M. A. Woodruff, *Macromol. Rapid Commun.* **2019**, *40*, 1900019.

[17] H. Ding, K. Cao, F. Zhang, W. Boettcher, R. C. Chang, *Mater. Des.* **2019**, *178*, 107857.

[18] G. Hochleitner, J. F. Hümmer, R. Luxenhofer, J. Groll, *Polymer (Guildf).* **2014**,

55, 5017.

[19] A. Hrynevich, Enhancement of Geometric Complexity and Predictability of Melt Electrowriting for Biomedical Applications, Julius-Maximilians-Universität Würzburg, **2020**.

[20] H. Lu, Y. Sun, Y. Chen, L. Nie, L. Yang, L. Du, H. Xu, *Mater. Lett.* **2022**, 133738.

[21] G. Hochleitner, F. Chen, C. Blum, P. D. Dalton, B. Amsden, J. Groll, *Acta Biomater.* **2018**, *72*, 110.

[22] M. Bergou, B. Audoly, E. Vouga, M. Wardetzky, E. Grinspun, *ACM Trans. Graph.* **2010**, *29*, 1.

[23] A. Hrynevich, I. Liashenko, P. D. Dalton, *Adv. Mater. Technol.* **2020**, *5*, 2000772.

[24] K. Cao, F. Zhang, B. Wang, Y. Sun, A. Zaeri, R. Zgeib, M. Mansouri, R. C. Chang, *Addit. Manuf.* **2022**, 103035.

[25] B. L. Devlin, S. Kuba, P. C. Hall, A. B. McCosker, E. Pickering, P. D. Dalton, T. J. Klein, M. A. Woodruff, N. C. Paxton, *Adv. Mater. Technol.* **2024**, DOI 10.1002/admt.202400419.

[26] A. Hrynevich, B. Ş. Elçi, J. N. Haigh, R. McMaster, A. Youssef, C. Blum, T. Blunk, G. Hochleitner, J. Groll, P. D. Dalton, *Small* **2018**, *14*, 1800232.

[27] P. Mieszczanek, T. M. Robinson, P. D. Dalton, D. W. Hutmacher, *Adv. Mater.* **2021**, 2100519.

[28] A. C. Abdullah, O. Ozarslan, S. S. Farshi, S. R. Dabbagh, S. Tasoglu, *Aggregate* **2024**, e495.

[29] F. M. Wunner, S. Eggert, J. Maartens, O. Bas, P. D. Dalton, E. M. De-Juan-Pardo, D. W. Hutmacher, *3D Print. Addit. Manuf.* **2019**, *6*, 82.

[30] F. M. Wunner, O. Bas, N. T. Saidy, P. D. Dalton, E. M. D.-J. Pardo, D. W. Hutmacher, *J. Vis. Exp.* **2017**, e56289.

[31] P. Mieszczanek, S. Eggert, P. Corke, D. W. Hutmacher, *HardwareX* **2021**, *e00246*.

[32] M. Lanaro, A. Luu, A. Lightbody-Gee, D. Hedger, S. K. Powell, D. W. Holmes, M.

A. Woodruff, *Int. J. Adv. Manuf. Technol.* **2021**, *113*, 2539.

[33] K. F. Eichholz, I. Gonçalves, X. Barceló, A. S. Federici, D. A. Hoey, D. J. Kelly, *Addit. Manuf.* **2022**, 102998.

[34] H. Xu, S. Fujiwara, L. Du, I. Liashenko, S. Luposchainsky, P. D. Dalton, *Polymer (Guildf).* **2024**, *309*, 127466.

[35] A. Reizabal, T. Kangur, P. G. Saiz, S. Menke, C. Moser, J. Brugger, P. D. Dalton, S. Luposchainsky, *Addit. Manuf.* **2023**, 103604.

[36] A. Zaeri, K. Cao, F. Zhang, R. Zgeib, R. C. Chang, *Macromol. Mater. Eng.* **2024**.

[37] F. Tourlomousis, H. Ding, D. M. Kalyon, R. C. Chang, *J. Manuf. Sci. Eng.* **2017**, *139*.

[38] P. G. Saiz, A. Reizabal, J. L. Vilas-Vilela, P. D. Dalton, S. Lanceros-Mendez, *Adv. Mater.* **2024**.

[39] F. Eberle, A.-K. Gruska, B. Filippi, P. Stahlhut, G. G. Wallace, P. D. Dalton, S. Beirne, *Adv. Eng. Mater.* **2022**, *24*, 2100750.

[40] B. Tandon, A. B. Züge, S. Luposchainsky, P. D. Dalton, *Adv. Eng. Mater.* **2023**.

[41] R. S. Diaz, E. M. De-Juan-Pardo, P. D. Dalton, T. R. Dargaville, *Macromol. Mater. Eng.* **2023**, *308*, 2200526.

[42] T. D. Brown, A. Slotosch, L. Thibaudeau, A. Taubenberger, D. Loessner, C. Vaquette, P. D. Dalton, D. W. Hutmacher, *Biointerphases* **2012**, *7*, 1.

[43] A. M. van Genderen, K. Jansen, M. Kristen, J. van Duijn, Y. Li, C. C. L. Schuurmans, J. Malda, T. Vermonden, J. Jansen, R. Masereeuw, *Front. Bioeng. Biotechnol.* **2021**, *8*, 1542.

[44] N. T. Saidy, A. Fernández-Colino, B. S. Heidari, R. Kent, M. Vernon, O. Bas, S. Mulderrig, A. Lubig, J. C. Rodríguez-Cabello, B. Doyle, D. W. Hutmacher, E. M. De-Juan-Pardo, P. Mela, *Adv. Funct. Mater.* **2022**, *32*, 2110716.

[45] T. D. Brown, F. Edin, N. Detta, A. D. Skelton, D. W. Hutmacher, P. D. Dalton, *Mater. Sci. Eng. C* **2014**, *45*, 698.

[46] J. N. Haigh, T. R. Dargaville, P. D. Dalton, *Mater. Sci. Eng. C* **2017**, *77*, 883.

[47] A. Reizabal, B. L. Devlin, N. C. Paxton, P. G. Saiz, I. Liashenko, S. Luposchainsky, M. A. Woodruff, S. L. Mendez, P. D. Dalton, *Macromol. Rapid Commun.* **2023**, 2300424.

[48] K. M. A. Mueller, A. Hangleiter, S. Burkhardt, D. M. Rojas-González, C. Kwade, S. T. Pammer, S. Leonhardt, P. Mela, *Small Sci.* **2023**, *3*, 2300021.

[49] Q. C. Peiffer, M. de Ruijter, J. van Duijn, D. Crottet, E. Dominic, J. Malda, M. Castilho, *Mater. Des.* **2020**, 109025.

[50] U. Saha, R. Nairn, O. Keenan, M. G. Monaghan, *Macromol. Mater. Eng.* **2021**, 2100496.

[51] Q. S. Thorsnes, P. R. Turner, M. A. Ali, J. D. Cabral, *Biomedicines* **2023**, *11*, 3139.

[52] N. T. Saidy, T. Shabab, O. Bas, D. M. Rojas-González, M. Menne, T. Henry, D. W. Hutmacher, P. Mela, E. M. De-Juan-Pardo, *Front. Bioeng. Biotechnol.* **2020**, *8*, 793.

[53] T. L. Brooks-Richards, N. C. Paxton, M. C. Allenby, M. A. Woodruff, *Mater. Des.* **2022**, *215*, 110466.

[54] M. Castilho, D. Feyen, M. Flandes-Iparraguirre, G. Hochleitner, J. Groll, P. A. F. Doevendans, T. Vermonden, K. Ito, J. P. G. Sluijter, J. Malda, *Adv. Healthc. Mater.* **2017**, *6*, 1700311.

[55] N. C. Paxton, M. Lanaro, A. Bo, N. Crooks, M. T. Ross, N. Green, K. Tetsworth, M. C. Allenby, Y. Gu, C. S. Wong, *J. Mech. Behav. Biomed. Mater.* **2020**, *105*, 103695.

[56] F. Zhang, K. Cao, A. Zaeri, R. Zgeib, R. C. Chang, *Macromol. Mater. Eng.* **2021**, 2200222.

[57] K. F. Eichholz, F. E. Freeman, P. Pitacco, J. Nulty, D. Ahern, R. Burdis, D. C. Browe, O. Garcia, D. A. Hoey, D. J. Kelly, *Biofabrication* **2022**, *14*, 45013.

[58] M. Shahverdi, S. Seifi, A. Akbari, K. Mohammadi, A. Shamloo, M. R. Movahhedy, *Sci. Rep.* **2022**, *12*, 1.

[59] E. McColl, J. Groll, T. Jungst, P. D. Dalton, *Mater. Des.* **2018**, *155*, 46.

[60] N. Pien, D. Di Francesco, F. Copes, M. Bartolf-Kopp, V. Chausse, M. Meeremans, M. Pegueroles, T. Jüngst, C. De Schauwer, F. Boccafoschi, *Front. Bioeng. Biotechnol.* **2023**, *11*.

[61] M. de Ruijter, A. Hrynevich, J. N. Haigh, G. Hochleitner, M. Castilho, J. Groll, J. Malda, P. D. Dalton, *Small* **2018**, *14*, 1702773.

[62] S. Luposchainsky, S. Jörissen, A. Nüchter, P. D. Dalton, *Macromol. Mater. Eng.* **2022**, 2200450.

[63] K. M. A. Mueller, A. Unterrainer, D. M. Rojas-González, E. De-Juan-Pardo, M. S. Willner, J. Herzen, P. Mela, *Adv. Mater. Technol.* **2023**, *8*, 2201158.

[64] E. Pickering, N. C. Paxton, A. Bo, B. O'Connell, M. King, M. A. Woodruff, *Adv. Eng. Mater.* **2022**, 2200479.

[65] A. B. McCosker, M. E. Snowdon, R. Lamont, M. A. Woodruff, N. C. Paxton, *Adv. Mater. Technol.* **2022**, *7*, 2200259.

[66] N. T. Saidy, F. Wolf, O. Bas, H. Keijdener, D. W. Hutmacher, P. Mela, E. M. De-Juan-Pardo, *Small* **2019**, *15*, 1900873.

[67] O. Bas, D. D'Angella, J. G. Baldwin, N. J. Castro, F. M. Wunner, N. T. Saidy, S. Kollmannsberger, A. Reali, E. Rank, E. M. De-Juan-Pardo, *ACS Appl. Mater. Interfaces* **2017**, *9*, 29430.

[68] N. C. Paxton, R. Daley, D. P. Forrestal, M. C. Allenby, M. A. Woodruff, *Mater. Des.* **2020**, 108787.

[69] D. Olvera, M. Sohrabi Molina, G. Hendy, M. G. Monaghan, *Adv. Funct. Mater.* **2020**, *30*, 1909880.

[70] M. J. Vernon, J. Lu, B. Padman, C. Lamb, R. Kent, P. Mela, B. Doyle, A. R. Ihdayhid, S. Jansen, R. J. Dilley, E. M. De-Juan-Pardo, *Adv. Healthc. Mater.* **2022**, *11*, 2201028.

[71] T. D. Brown, P. D. Dalton, D. W. Hutmacher, *Prog. Polym. Sci.* **2016**, *56*, 116.

[72] G. C. Rutledge, S. V. Fridrikh, *Adv. Drug Deliv. Rev.* **2007**, *59*, 1384.

[73] J. Rnjak-Kovacina, A. S. Weiss, *Tissue Eng. Part B Rev.* **2011**, *17*, 365.

[74] S. J. Eichhorn, W. W. Sampson, *J. R. Soc. Interface* **2005**, *2*, 309.

[75] D. Palomares, K. R. Ammann, J. J. Saldana Perez, A. Gomez, A. Barreda, A. Russell-Cheung, A. Martin, P. Le Tran, S. Hossainy, R. C. Slepian, S. F. A. Hossainy, M. J. Slepian, *ACS Appl. Bio Mater.* **2021**, *4*, 4084.

[76] W. E. Teo, S. Ramakrishna, *Nanotechnology* **2006**, *17*, R89.

[77] B. N. Turner, S. A. Gold, *Rapid Prototyp. J.* **2015**, *21*, 250.

[78] A. Cano-Vicent, M. M. Tambuwala, S. S. Hassan, D. Barh, A. A. A. Aljabali, M. Birkett, A. Arjunan, Á. Serrano-Aroca, *Addit. Manuf.* **2021**, *47*, 102378.

[79] L. Romero, A. Guerrero, M. M. Espinosa, M. Jiménez, I. A. Domínguez, M. Domínguez, in *25th Annu. Int. Solid Free. Fabr. Symp.*, **2014**, pp. 120–131.

[80] C. Böhm, P. Stahlhut, J. Weichhold, A. Hrynevich, J. Teßmar, P. D. Dalton, *Small* **2022**, *18*, 2104193.

[81] C. Böhm, B. Tandon, A. Hrynevich, J. Teßmar, P. D. Dalton, *Macromol. Chem. Phys.* **2022**, *223*, 2100417.

[82] C. D. O'Connell, O. Bridges, C. Everett, N. Antill-O'Brien, C. Onofrillo, C. Di Bella, *Adv. Mater. Technol.* **2021**, 2100345.

[83] Z. Liu, J. Jia, Q. Lei, Y. Wei, Y. Hu, X. Lian, L. Zhao, X. Xie, H. Bai, X. He, L. Si, C. Livermore, R. Kuang, Y. Zhang, J. Wang, Z. Yu, X. Ma, D. Huang, *Adv. Healthc. Mater.* **2024**.

[84] T. B. Wissing, V. Bonito, C. V. C. Bouten, A. I. P. M. Smits, *NPJ Regen. Med.* **2017**, *2*, 1.

[85] T. Jungst, I. Pennings, M. Schmitz, A. J. W. P. Rosenberg, J. Groll, D. Gawlitta, *Adv. Funct. Mater.* **2019**, *29*, 1905987.

[86] A. S. Federici, O. Garcia, D. J. Kelly, D. A. Hoey, *Adv. Funct. Mater.* **2024**.

[87] J. Kim, E. Bakirci, K. L. O'Neill, A. Hrynevich, P. D. Dalton, *Macromol. Mater. Eng.* **2021**, 2000685.

[88] S. J. Hollister, *Adv. Mater.* **2009**, *21*, 3330.

[89] P. Zilla, D. Bezuidenhout, P. Human, *Biomaterials* **2007**, *28*, 5009.

[90] B. Mirani, S. O. Mathew, N. Latifi, M. R. Labrosse, B. G. Amsden, C. A.

Simmons, *Adv. Funct. Mater.* **2023**.

[91] M. Bartolf-Kopp, L. de Silva, A. J. W. P. Rosenberg, J. Groll, D. Gawlitta, T. Jungst, *Adv. Funct. Mater.* **2024**, DOI 10.1002/adfm.202311797.

[92] A. A. Appel, M. A. Anastasio, J. C. Larson, E. M. Brey, *Biomaterials* **2013**, *34*, 6615.

[93] J. Wahsner, E. M. Gale, A. Rodríguez-Rodríguez, P. Caravan, *Chem. Rev.* **2018**, *119*, 957.

[94] A. Bîrcă, O. Gherasim, V. Grumezescu, A. M. Grumezescu, in *Mater. Biomed. Eng.*, Elsevier, **2019**, pp. 1–28.

[95] S. Ray, R. P. Cooney, in *Handb. Environ. Degrad. Mater.*, Elsevier, **2018**, pp. 185–206.

[96] M. Labet, W. Thielemans, *Chem. Soc. Rev.* **2009**, *38*, 3484.

[97] M. A. Woodruff, D. W. Hutmacher, *Prog. Polym. Sci.* **2010**, *35*, 1217.

[98] M. Bartnikowski, T. R. Dargaville, S. Ivanovski, D. W. Hutmacher, *Prog. Polym. Sci.* **2019**, *96*, 1.

[99] J. C. Kade, P. D. Dalton, *Adv. Healthc. Mater.* **2021**, *10*, 2001232.

[100] S. A. M. Ali, S.-P. Zhong, P. J. Doherty, D. F. Williams, *Biomaterials* **1993**, *14*, 648.

[101] G. P. Sailema-Palate, A. Vidaurre, A. J. Campillo-Fernández, I. Castilla-Cortázar, *Polym. Degrad. Stab.* **2016**, *130*, 118.

[102] J. H. Jung, M. Ree, H. Kim, *Catal. Today* **2006**, *115*, 283.

[103] C. E. T. Stowell, Y. Wang, *Biomaterials* **2018**, *173*, 71.

[104] H.-J. Sung, C. Meredith, C. Johnson, Z. S. Galis, *Biomaterials* **2004**, *25*, 5735.

[105] J. A. Martins, A. A. Lach, H. L. Morris, A. J. Carr, P.-A. Mouthuy, *J. Biomater. Appl.* **2020**, *34*, 902.

[106] H. R. Kricheldorf, D.-O. Damrau, *Macromol. Chem. Phys.* **1998**, *199*, 1089.

[107] J. A. Ray, N. Doddi, D. Regula, J. A. Williams, A. Melveger, *Surg. Gynecol.*

Obstet. **1981**, *153*, 497.

[108] H. J. Kang, Y. S. Song, *Polym. Eng. Sci.* **2022**, *62*, 2070.

[109] J. Zhang, S. Jones, D. Wang, A. Wood, T. Washington, K. Acreman, B. Cuevas, A. Karau, *Polym. Eng. Sci.* **2019**, *59*, 1701.

[110] X. Feng, L. Wang, Z. Xue, C. Xie, J. Han, Y. Pei, Z. Zhang, W. Guo, B. Lu, *Sci. Adv.* **2024**, *10*.

[111] W. S. Skinner, P. G. Saiz, A. Reizabal, J. E. Plumley, P. D. Dalton, K. G. Ong, *Sensors & Diagnostics* **2024**.

[112] O. Bas, B. Gorissen, S. Luposchainsky, T. Shabab, K. Bertoldi, D. W. Hutmacher, *Multifunct. Mater.* **2021**, *4*, 45001.

[113] A. Roschli, K. T. Gaul, A. M. Boulger, B. K. Post, P. C. Chesser, L. J. Love, F. Blue, M. Borish, *Addit. Manuf.* **2019**, *25*, 275.

[114] X. Gao, S. Qi, X. Kuang, Y. Su, J. Li, D. Wang, *Addit. Manuf.* **2021**, *37*, 101658.

[115] M. F. Arif, S. Kumar, K. M. Varadarajan, W. J. Cantwell, *Mater. Des.* **2018**, *146*, 249.

[116] M. Vaezi, S. Yang, *Virtual Phys. Prototyp.* **2015**, *10*, 123.

[117] S. Y. Sonaye, J. P. Mack, K.-T. Tan, J. S. Owusu-Danquah, P. Sikder, *Prog. Addit. Manuf.* **2024**.

[118] P. Wang, B. Zou, H. Xiao, S. Ding, C. Huang, *J. Mater. Process. Technol.* **2019**, *271*, 62.

[119] C. Zawaski, C. Williams, *Addit. Manuf.* **2020**, *33*, 101111.

[120] C. Basgul, F. M. Thieringer, S. M. Kurtz, *Addit. Manuf.* **2021**, *46*, 102097.

[121] T. Liu, M. Zhang, Y. Kang, X. Tian, J. Ding, D. Li, *Addit. Manuf.* **2023**, *62*, 103390.

[122] C. Bellehumeur, L. Li, Q. Sun, P. Gu, *J. Manuf. Process.* **2004**, *6*, 170.

[123] S. Singh, G. Singh, C. Prakash, S. Ramakrishna, *J. Manuf. Process.* **2020**, *55*, 288.

[124] F. Zhang, L. Zhu, Z. Li, S. Wang, J. Shi, W. Tang, N. Li, J. Yang, *Addit. Manuf.* **2021**, *48*, 102423.

[125] A. Al Rashid, W. Ahmed, M. Y. Khalid, M. Koç, *Addit. Manuf.* **2021**, *47*, 102279.

[126] M. Schuster, C. Turecek, B. Kaiser, J. Stampfl, R. Liska, F. Varga, *J. Macromol. Sci. Part A* **2007**, *44*, 547.

[127] F. P. W. Melchels, J. Feijen, D. W. Grijpma, *Biomaterials* **2010**, *31*, 6121.

[128] E. C. Gugua, C. O. Ujah, C. O. Asadu, D. V. Von Kallon, B. N. Ekwueme, *Hybrid Adv.* **2024**, *7*, 100286.

[129] D. F. Williams, *Biomaterials* **2008**, *29*, 2941.

[130] International Organization for Standardization, **2009**, ISO 10993:5.

[131] T. Mosmann, *J. Immunol. Methods* **1983**, *65*, 55.

[132] International Organization for Standardization, **2017**, ISO 10993:4.

[133] M. Quirynen, S. A. M. Siawasch, J. Yu, R. J. Miron, *Periodontol. 2000* **2024**, DOI 10.1111/prd.12555.

[134] R. A. Malinauskas, *Artif. Organs* **1997**, *21*, 1255.

[135] ASTM Interantional, **2017**, ASTM F756 Standard Practice for Assessment of Hemo.

[136] L.-C. Xu, J. W. Bauer, C. A. Siedlecki, *Colloids Surfaces B Biointerfaces* **2014**, *124*, 49.

[137] D. Green, *Hemodial. Int.* **2006**, *10*.

[138] B. A. Bouchard, J. R. Silveira, P. B. Tracy, in *Platelets*, Elsevier, **2013**, pp. 425–451.

[139] H. Sinno, S. Prakash, *Plast. Surg. Int.* **2013**, *2013*, 1.

[140] J. F. van Velzen, B. A. P. Laros-van Gorkom, G. A. M. Pop, W. L. van Heerde, *Thromb. Res.* **2012**, *130*, 92.

[141] L. Tang, C. Liu, P. Rosenberger, *Front. Immunol.* **2023**, *14*.

[142] L. J. Sharman, R. H. Sones, L. H. Cragg, *J. Appl. Phys.* **1953**, *24*, 703.

[143] H. J. Butler, L. Ashton, B. Bird, G. Cinque, K. Curtis, J. Dorney, K. Esmonde-White, N. J. Fullwood, B. Gardner, P. L. Martin-Hirsch, M. J. Walsh, M. R. McAinsh, N. Stone, F. L. Martin, *Nat. Protoc.* **2016**, *11*, 664.

[144] C. V. Raman, K. S. Krishnan, *Nature* **1928**, *122*, 12.

[145] International Organization for Standardization, **2019**, ISO 527.

[146] J. R. Davis, Ed. , *Tensile Testing*, ASTM International, **2004**.

[147] G. M. Swallowe, in *Mech. Prop. Test. Polym.*, **1999**, pp. 214–218.

[148] P. C. Goodwin, *Mol. Reprod. Dev.* **2015**, *82*, 502.

[149] R. F. Egerton, *Physical Principles of Electron Microscopy*, Springer, **2005**.

[150] E. S. Statnik, A. I. Salimon, A. M. Korsunsky, *Mater. Today Proc.* **2020**, *33*, 1917.

[151] J. W. Lichtman, J.-A. Conchello, *Nat. Methods* **2005**, *2*, 910.

[152] J. Kapuscinski, *Biotech. Histochem.* **1995**, *70*, 220.

[153] A. E. M. Adams, J. R. Pringle, in *Methods Enzymol.*, **1991**, pp. 729–731.

[154] E. H. Beutner, *Bacteriol. Rev.* **1961**, *25*, 49.

[155] S. Wischnitzer, *Introduction to Electron Microscopy*, **1953**.

[156] T. M. Buzug, in *Springer Handb. Med. Technol.*, Springer Berlin Heidelberg, Berlin, Heidelberg, **2011**, pp. 311–342.

[157] G. N. Hounsfield, *Science* **1980**, *210*, 22.

[158] E. Moser, A. Stadlbauer, C. Windischberger, H. H. Quick, M. E. Ladd, *Eur. J. Nucl. Med. Mol. Imaging* **2009**, *36*, 30.

[159] E. L. Hahn, *Phys. Rev.* **1950**, *77*, 297.

[160] I. Tirotta, V. Dichiarante, C. Pigliacelli, G. Cavallo, G. Terraneo, F. B. Bombelli, P. Metrangolo, G. Resnati, *Chem. Rev.* **2015**, *115*, 1106.

[161] International Organization for Standardization, **2017**, ISO 7198.

[162] M. Stoiber, C. Grasl, F. Moscato, H. Schima, in *Tissue-Engineered Vasc. Grafts*, Springer International Publishing, Cham, **2020**, pp. 1–28.

[163] P. Terranova, K. M. A. Mueller, D. Biebl, A. D'Amore, P. Mela, *Addit. Manuf.* **2024**, *93*, 104431.

[164] D. Vervoort, A. Malik, S. E. Fremes, *JTCVS Tech.* **2021**, *10*, 102.

[165] S. Lampridis, S. J. George, *Ann. Thorac. Surg.* **2021**, *112*, 2094.

[166] S. Pashneh-Tala, S. MacNeil, F. Claeyssens, *Tissue Eng. Part B Rev.* **2016**, *22*, 68.

[167] H.-H. G. Song, R. T. Rumma, C. K. Ozaki, E. R. Edelman, C. S. Chen, *Cell Stem Cell* **2018**, *22*, 340.

[168] B. J. de Kort, S. E. Koch, T. B. Wissing, M. M. Krebber, C. V. C. Bouten, A. Smits, *Adv. Drug Deliv. Rev.* **2021**, 113960.

[169] L. Li, C. M. Terry, Y.-T. E. Shiu, A. K. Cheung, *Kidney Int.* **2008**, *74*, 1247.

[170] P. Roy-Chaudhury, B. S. Kelly, M. A. Miller, A. Reaves, J. Armstrong, N. Nanayakkara, S. C. Heffelfinger, *Kidney Int.* **2001**, *59*, 2325.

[171] H. Haruguchi, S. Teraoka, *J. Artif. Organs* **2003**, *6*, 227.

[172] C. A. Best, J. M. Szafron, K. A. Rocco, J. Zbinden, E. W. Dean, M. W. Maxfield, H. Kurobe, S. Tara, P. S. Bagi, B. V Udelsman, *Acta Biomater.* **2019**, *94*, 183.

[173] T. Sologashvili, S. A. Saat, J.-C. Tille, S. De Valence, D. Mugnai, J. P. Giliberto, J. Dillon, A. Yakub, Z. Dimon, R. Gurny, *Eur. J. Pharm. Biopharm.* **2019**, *139*, 272.

[174] C. Spadaccio, F. Nappi, N. Al-Attar, F. W. Sutherland, C. Acar, A. Nenna, M. Trombetta, M. Chello, A. Rainer, *J. Cardiovasc. Transl. Res.* **2016**, *9*, 334.

[175] K. M. A. Mueller, S. Mansi, E. M. De-Juan-Pardo, P. Mela, *Front. Bioeng. Biotechnol.* **2024**, *12*.

[176] G. Zhang, W. Li, M. Yu, H. Huang, Y. Wang, Z. Han, K. Shi, L. Ma, Z. Yu, X. Zhu, *Adv. Sci.* **2023**, 2206264.

[177] M. Castilho, A. van Mil, M. Maher, C. H. G. Metz, G. Hochleitner, J. Groll, P. A.

Doevendans, K. Ito, J. P. G. Sluijter, J. Malda, *Adv. Funct. Mater.* **2018**, *28*, 1803151.

[178] M. J. Ainsworth, N. Chirico, M. de Ruijter, A. Hrynevich, I. Dokter, J. P. G. Sluijter, J. Malda, A. van Mil, M. Castilho, *Biofabrication* **2023**.

[179] K. Han, J. He, L. Fu, M. Mao, Y. Kang, D. Li, *Biofabrication* **2022**, *15*, 15003.

[180] P. Montero-Calle, M. Flandes-Iparraguirre, K. Mountris, A. S de la Nava, N. Laita, R. M. Rosales, O. Iglesias-García, E. M. De-Juan-Pardo, F. Atienza, M. E. Fernández-Santos, E. Peña, M. Doblaré, J. J. Gavira, F. Fernández-Avilés, F. Prósper, E. Pueyo, M. M. Mazo, *Biofabrication* **2022**, *14*, 045017.

[181] A. Weekes, J. M. Wasielewska, N. Pinto, J. Jenkins, J. Patel, Z. Li, T. J. Klein, C. Meinert, *J. Tissue Eng. Regen. Med.* **2024**, *2024*.

[182] M. Bartolf-Kopp, T. Jungst, *Adv. Healthc. Mater.* **2024**.

[183] A. S. Federici, B. Tornifoglio, C. Lally, O. Garcia, D. J. Kelly, D. A. Hoey, *J. Mech. Behav. Biomed. Mater.* **2023**, 106292.

[184] D. Zhi, Q. Cheng, A. C. Midgley, Q. Zhang, T. Wei, Y. Li, T. Wang, T. Ma, M. Rafique, S. Xia, *Sci. Adv.* **2022**, *8*, eabl3888.

[185] A. Weekes, G. Wehr, N. Pinto, J. Jenkins, Z. Li, C. Meinert, T. J. Klein, *Biofabrication* **2023**.

[186] Y. Chen, Z. Zou, T. Fu, Z. Li, Z. Zhang, M. Zhu, Q. Gao, S. Wu, G. Fu, Y. He, J. Fu, *Int. J. Extrem. Manuf.* **2024**, *6*, 035503.

[187] A. Fernández-Colino, F. Wolf, S. Rütten, T. Schmitz-Rode, J. C. Rodríguez-Cabello, S. Jockenhoevel, P. Mela, *Front. Bioeng. Biotechnol.* **2019**, *7*, 340.

[188] J. A. Shaw, B. A. Kingwell, A. S. Walton, J. D. Cameron, P. Pillay, C. D. Gatzka, A. M. Dart, *J. Am. Coll. Cardiol.* **2002**, *39*, 1637.

[189] C. J. van Andel, P. V Pistecky, C. Borst, *Ann. Thorac. Surg.* **2003**, *76*, 58.

[190] S. Laurent, B. Caviezel, L. Beck, X. Girerd, E. Billaud, P. Boutouyrie, A. Hoeks, M. Safar, *Hypertension* **1994**, *23*, 878.

[191] S. E. Greenwald, C. L. Berry, *J. Pathol.* **2000**, 292.

[192] N. R. M. Tai, A. Giudiceandrea, H. J. Salacinski, A. M. Seifalian, G. Hamilton, *J. Vasc. Surg.* **1999**, *30*, 936.

[193] G. Konig, T. N. McAllister, N. Dusserre, S. A. Garrido, C. Iyican, A. Marini, A. Fiorillo, H. Avila, W. Wystrychowski, K. Zagalski, M. Maruszewski, A. L. Jones, L. Cierpka, L. M. de la Fuente, N. L'Heureux, *Biomaterials* **2009**, *30*, 1542.

[194] S. G. Wise, M. J. Byrom, A. Waterhouse, P. G. Bannon, M. K. C. Ng, A. S. Weiss, *Acta Biomater.* **2011**, *7*, 295.

[195] V. A. Kumar, L. P. Brewster, J. M. Caves, E. L. Chaikof, *Cardiovasc. Eng. Technol.* **2011**, *2*, 137.

[196] R. Roeder, J. Wolfe, N. Lianakis, T. Hinson, L. A. Geddes, J. Obermiller, *J. Biomed. Mater. Res.* **1999**, *47*, 65.

[197] N. L'Heureux, N. Dusserre, G. Konig, B. Victor, P. Keire, T. N. Wight, N. A. F. Chronos, A. E. Kyles, C. R. Gregory, G. Hoyt, *Nat. Med.* **2006**, *12*, 361.

[198] S. Sarkar, H. J. Salacinski, G. Hamilton, A. M. Seifalian, *Eur. J. Vasc. Endovasc. Surg.* **2006**, *31*, 627.

[199] N. R. Tai, H. J. Salacinski, A. Edwards, G. Hamilton, A. M. Seifalian, *Br. J. Surg.* **2002**, *87*, 1516.

[200] M. Tozzi, J. De Letter, D. Krievins, J. Jushinskis, A. D'Haeninck, K. Rucinskas, M. Miglinas, T. Baltrunas, S. Nauwelaers, A. S. De Vriese, F. Moll, F. Vermassen, *J. Vasc. Access* **2024**.

[201] P. J. Besseling, W. Szymczyk, M. Teraa, R. J. Toorop, D. J. Wu, R. C. H. Driessen, A. M. Lichauco, H. M. Janssen, M. van de Kaa, K. den Ouden, P. M. de Bree, J. O. Fledderus, C. V. C. Bouten, G. J. de Borst, P. Y. W. Dankers, M. C. Verhaar, *Adv. Healthc. Mater.* **2024**.

[202] N. Davidenko, C. F. Schuster, D. V. Bax, R. W. Farndale, S. Hamaia, S. M. Best, R. E. Cameron, *J. Mater. Sci. Mater. Med.* **2016**, *27*, 148.

[203] A. Krüger-Genge, S. Hauser, A. T. Neffe, Y. Liu, A. Lendlein, J. Pietzsch, F. Jung, *ACS Biomater. Sci. Eng.* **2021**, *7*, 527.

[204] K. H. Hussein, K.-M. Park, K.-S. Kang, H.-M. Woo, *Acta Biomater.* **2016**, *38*, 82.

[205] S. Nakamura, T. Kubo, H. Ijima, *J. Biosci. Bioeng.* **2013**, *115*, 562.

[206] S. R. Klein, *Arch. Surg.* **1982**, *117*, 45.

[207] M. B. Detweiler, J. G. Detweiler, J. Fenton, *J. Investig. Surg.* **1999**, *12*, 245.

[208] J. G. Ribaudo, K. He, S. Madira, E. R. Young, C. Martin, T. Lu, J. M. Sacks, X. Li, *Bioact. Mater.* **2024**, *38*, 73.

[209] D. J. Wu, K. van Dongen, W. Szymczyk, P. J. Besseling, R. M. Cardinaels, G. Marchioli, M. H. P. van Genderen, C. V. C. Bouten, A. I. P. M. Smits, P. Y. W. Dankers, *Front. Mater.* **2020**, *7*.

[210] J. Schmidli, M. K. Widmer, C. Basile, G. de Donato, M. Gallieni, C. P. Gibbons, P. Haage, G. Hamilton, U. Hedin, L. Kamper, M. K. Lazarides, B. Lindsey, G. Mestres, M. Pegoraro, J. Roy, C. Setacci, D. Shemesh, J. H. M. Tordoir, M. van Loon, ESVS Guidelines Committee, P. Kolh, G. J. de Borst, N. Chakfe, S. Debus, R. Hinchliffe, S. Kakkos, I. Koncar, J. Lindholt, R. Naylor, M. Vega de Ceniga, F. Vermassen, F. Verzini, ESVS Guidelines Reviewers, M. Mohaupt, J.-B. Ricco, R. Roca-Tey, *Eur. J. Vasc. Endovasc. Surg.* **2018**, *55*, 757.

[211] C. E. Lok, T. S. Huber, T. Lee, S. Shenoy, A. S. Yevzlin, K. Abreo, M. Allon, A. Asif, B. C. Astor, M. H. Glickman, J. Graham, L. M. Moist, D. K. Rajan, C. Roberts, T. J. Vachharajani, R. P. Valentini, *Am. J. Kidney Dis.* **2020**, *75*, S1.

[212] L. C. Bylsma, S. M. Gage, H. Reichert, S. L. M. Dahl, J. H. Lawson, *Eur. J. Vasc. Endovasc. Surg.* **2017**, *54*, 513.

[213] M. K. Lazarides, G. S. Georgiadis, G. A. Antoniou, D. N. Staramos, *J. Vasc. Surg.* **2007**, *45*, 420.

[214] K. Woo, D. P. Goldman, J. A. Romley, *Clin. J. Am. Soc. Nephrol.* **2015**, *10*, 1791.

[215] R. S. Brown, B. K. Patibandla, A. S. Goldfarb-Rumyantzev, *J. Am. Soc. Nephrol.* **2017**, *28*, 645.

[216] D. E. Disbrow, D. L. Cull, C. G. Carsten, S. K. Yang, B. L. Johnson, G. P. Keahey, *J. Am. Coll. Surg.* **2013**, *216*, 679.

[217] Z. J. Haskal, S. Trerotola, B. Dolmatch, E. Schuman, S. Altman, S. Mietling, S. Berman, G. McLennan, C. Trimmer, J. Ross, T. Vesely, *N. Engl. J. Med.* **2010**, *362*, 494.

[218] F. J. Albers, *Adv. Ren. Replace. Ther.* **1994**, *1*, 107.

[219] F. Zhang, K. Cao, A. Zaeri, R. Zgeib, R. C. Chang, *J. Appl. Polym. Sci.* **n.d.**, 52235.

[220] G. Zhang, Y. Xu, Y. Sun, X. Ye, L. Du, H. Xu, *Langmuir* **2023**.

[221] M. K. Włodarczyk-Biegun, M. Villiou, M. Koch, C. Muth, P. Wang, J. Ott, A. Del Campo, *ACS Biomater. Sci. Eng.* **2022**.

[222] N. Abbasi, A. Abdal-Hay, S. Hamlet, E. Graham, S. Ivanovski, *ACS Biomater. Sci. Eng.* **2019**, *5*, 3448.

[223] ASTM International, **2017**, ASTM F 756.

[224] F. Wolf, D. M. Rojas González, U. Steinseifer, M. Obdenbusch, W. Herfs, C. Brecher, S. Jockenhoevel, P. Mela, T. Schmitz-Rode, *Ann. Biomed. Eng.* **2018**, *46*, 616.

[225] J. Schindelin, I. Arganda-Carreras, E. Frise, V. Kaynig, M. Longair, T. Pietzsch, S. Preibisch, C. Rueden, S. Saalfeld, B. Schmid, *Nat. Methods* **2012**, *9*, 676.

[226] C. A. Schneider, W. S. Rasband, K. W. Eliceiri, *Nat. Methods* **2012**, *9*, 671.

[227] K. M. A. Mueller, G. J. Topping, S. P. Schwaminger, Y. Zou, D. M. Rojas-González, E. M. De-Juan-Pardo, S. Berensmeier, F. Schilling, P. Mela, *Biomater. Sci.* **2021**, *9*, 4607.

[228] I. Gibson, D. Rosen, B. Stucker, M. Khorasani, *Additive Manufacturing Technologies*, Springer New York, New York, NY, **2021**.

[229] G. Sacks, V. Shah, L. Yao, C. Yan, D. Shah, L. Limeta, V. DeStefano, *Biomed. Technol.* **2024**, *6*, 75.

[230] A. García-Collado, J. M. Blanco, M. K. Gupta, R. Dorado-Vicente, *Addit. Manuf.* **2022**, *50*, 102577.

[231] M. Castilho, M. de Ruijter, S. Beirne, C. C. Villette, K. Ito, G. G. Wallace, J. Malda, *Trends Biotechnol.* **2020**, *38*, 1316.

[232] M. H. Yacoub, Y.-T. Tseng, J. Kluin, A. Vis, U. Stock, H. Smail, P. Sarathchandra, E. Aikawa, H. El-Nashar, A. H. Chester, N. Shehata, M. Nagy, A. El-sawy, W. Li, G. Burriesci, J. Salmonsmith, S. Romeih, N. Latif, *Commun. Biol.*

2023, *6*, 1017.

[233] Z. Prodan, T. Mroczek, S. Sivalingam, G. Bennink, F. M. Asch, M. Cox, T. Carrel, M. A. Yakub, Z. Nagy, J. Skalski, O. Svanidze, E. Schutte, L. Verhees, C. Klersy, R. Virmani, N. Sreeram, *Semin. Thorac. Cardiovasc. Surg.* **2022**, *34*, 985.

[234] D. L. Morales, C. Herrington, E. A. Bacha, V. O. Morell, Z. Prodán, T. Mroczek, S. Sivalingam, M. Cox, G. Bennink, F. M. Asch, *Front. Cardiovasc. Med.* **2021**, *7*.

[235] M. Thubrikar, *The Aortic Valve*, Routledge, **2018**.

[236] G. G. Belz, *Cardiovasc. Drugs Ther.* **1995**, *9*, 73.

[237] C. G. Pitt, F. I. Chasalow, Y. M. Hibionada, D. M. Klimas, A. Schindler, *J. Appl. Polym. Sci.* **1981**, *26*, 3779.

[238] W. Wu, R. A. Allen, Y. Wang, *Nat. Med.* **2012**, *18*, 1148.

Scientific Output

List of Peer-reviewed Publications

Kilian M. A. Mueller, Geoffrey J. Topping, Sebastian P. Schwaminger, Yunzhe Zou, Diana M. Rojas-González, Elena M. De-Juan-Pardo, Sonja Berensmeier, Franz Schilling, Petra Mela. *Visualization of USPIO-labeled Melt-electrowritten Scaffolds by Non-invasive Magnetic Resonance Imaging,* Biomaterials Science 9:13, 2021.

Kilian M. A. Mueller, Shane Mulderrig, Sara Najafian, Samuel Benjamin Hurvitz, Deepanshu Sodhani, Petra Mela, Scott Edward Stapleton. *Mesh Manipulation for Local Structural Property Tailoring of Medical Warp-knitted Textiles,* Journal of the Mechanical Behavior of Biomedical Materials 128, 2022.

Kilian M. A. Mueller, Sebastian T. Pammer, Stefan Leonhardt, Petra Mela. *A Feature Specific Local Cooling System to Control Tensile Strength and Dimensional Accuracy in Fused Filament Fabrication,* 3D Printing and Additive Manufacturing 10:1, 2023.

Kilian M. A. Mueller, Andreas Unterrainer, Diana M. Rojas-González, Elena M. De-Juan-Pardo, Marian S. Willner, Julia Herzen, Petra Mela*. Introducing Controlled Microporosity in Melt Electrowriting,* Advanced Materials Technologies 8:6, 2023.

Kilian M. A. Mueller*, Annika Hangleiter*, Sarah Burkhardt, Diana M. Rojas-González, Christina Kwade, Sebastian T. Pammer, Stefan Leonhardt, Petra Mela. *Filament-based Melt Electrowriting Enables Dual Mode Additive Manufacturing for Multiscale Constructs,* Small Science 3:8, 2023. * equal contribution

Salma Mansi, Sarah Dummert, Geoffrey J. Topping, Mian Zahid Hussain, Carolin Rickert, **Kilian M. A. Mueller**, Tim Kratky, Martin Elsner, Angela Casini, Franz Schilling, Roland A. Fischer, Oliver Lieleg, Petra Mela. *Introducing Metal-Organic Frameworks to Melt Electrowriting: Multifunctional Scaffolds with Controlled Microarchitecture for Tissue Engineering Applications,* Advanced Functional Materials 34:2, 2024.

Kilian M. A. Mueller, Salma Mansi, Elena M. De-Juan-Pardo, Petra Mela. *Advances in Melt Electrowriting for Cardiovascular Applications.* Frontiers in Bioengineering and Biotechnology 12, 2024.

Pietro Terranova*, **Kilian M. A. Mueller***, Dominic Biebl, Antonio D'Amore, Petra Mela. *A Versatile 5-Axis Melt Electrowriting Platform for Unprecedented Design Freedom of 3D Fibrous Scaffolds*, Additive Manufacturing 93, 2024. * equal contribution

Conference Contributions

Kilian M. A. Mueller, Geoffrey J. Topping, Sebastian P. Schwaminger, Yunzhe Zou, Diana M. Rojas-González, Elena M. De-Juan-Pardo, Sonja Berensmeier, Franz Schilling, Petra Mela. *Melt-Electrowritten Scaffolds with Ultrasmall Superparamagnetic Iron Oxide Nanoparticles as Contrast Agent for Non-Invasive Magnetic Resonance Imaging,* 31st Conference of the European Society for Biomaterials (ESB): Porto (virtual), 2021, poster presentation.

Geoffrey J. Topping*, **Kilian M. A. Mueller***, Sebastian P. Schwaminger, Yunzhe Zou, Diana M. Rojas-González, Elena M. De-Juan-Pardo, Sonja Berensmeier, Petra Mela, Franz Schilling. *MRI Relaxometry of USPIO-Labeled Melt-Electrowritten Scaffolds,* 16th European Molecular Imaging Meeting (EMIM): Göttingen, 2021, oral presentation. * equal contribution

Kilian M. A. Mueller, Geoffrey J. Topping, Sebastian P. Schwaminger, Yunzhe Zou, Diana M. Rojas-González, Elena M. De-Juan-Pardo, Sonja Berensmeier, Franz Schilling, Petra Mela. *Magnetic Resonance Imaging of USPIO-Labeled Melt-Electrowritten Polycaprolactone Scaffolds,* Annual Meeting of the German Society for Biomaterials (DGBM): virtual, 2021, oral presentation.

Kilian M. A. Mueller, Geoffrey J. Topping, Sebastian P. Schwaminger, Yunzhe Zou, Diana M. Rojas-González, Elena M. De-Juan-Pardo, Sonja Berensmeier, Franz Schilling, Petra Mela. *Towards Clinical Translation of Melt-Electrowritten Scaffolds: Visualization of USPIO-labeled Polycaprolactone Scaffolds by Magnetic Resonance Imaging,* 12th European Symposium on Vascular Biomaterials (ESVB): Straßbourg, 2021, oral presentation.

Kilian M. A. Mueller, Andreas Unterrainer, Diana M. Rojas-González, Petra Mela. *Digital Fabrication of Highly Tunable Anisotropic Scaffolds for In Situ Heart Valve Tissue Engineering via Melt Electrowriting,* Heart Valve Society Annual Meeting (HVS): Miami, 2022, oral presentation.

Marina Kühn-Kauffeldt, Marvin Kühn, **Kilian M. A. Mueller**, Petra Mela. *3D Printing in Vacuum - A Novel Approach for Additive Manufacturing of High-Performance Polymers,* 1st International Conference on Advanced Manufacturing for Air, Space and Land Transportation (ICAM): virtual, 2022, oral presentation.

Kilian M. A. Mueller, Andreas Unterrainer, Diana M. Rojas-González, Marian Willner, Julia Herzen, Petra Mela, *Melt-Electrowritten Highly Tunable Anisotropic Scaffolds for Cardiovascular Tissue Engineering*, Tissue Engineering and Regenerative Medicine International Society (TERMIS) European Chapter Conference: Krakow, 2022, oral presentation.

Sarah Burkhardt, Christina Kwade, **Kilian M. A. Mueller**, Petra Mela, *Melt Electrowriting for Tuning the Properties of Implant Surfaces,* Tissue Engineering and Regenerative Medicine International Society (TERMIS) European Chapter Conference: Krakow, 2022, oral presentation.

Kilian M. A. Mueller, Andreas Unterrainer, Diana Marcela Rojas-González, Marian Willner, Julia Herzen, Petra Mela, *Introducing Controlled Microporosity to Melt Electrowriting: Tuning Pore Morphology and Anisotropy,* International Conference on Biofabrication: Pisa, 2022, oral presentation.

Geoffrey J. Topping, Salma Mansi, **Kilian M. A. Mueller**, Zahid Hussain, Sarah Dummert, Carolin Rickert, Sebastian P. Schwaminger, Yunzhe Zou, Diana M. Rojas-González, Sonja Berensmeier, Oliver Lieleg, Roland Fischer, Petra Mela, Franz Schilling, *Relaxation Rate MR Contrast of Metal-Organic Framework or USPIO Labelled Melt-Electrowritten Polycaprolactone Scaffolds,* ISMRM & ISMRT Annual Meeting: Toronto, 2023, poster presentation.

Salma Mansi, Zahid Hussain, Geoffrey J. Topping, Sarah Dummert, Carolin Rickert, **Kilian M. A. Mueller**, Franz Schilling, Roland Fischer, Oliver Lieleg, Petra Mela, *Multifunctional Scaffolds by Melt Electrowriting Metal-Organic Framework / Polycaprolactone Composites for Tissue Engineering Applications,* 13th European Symposium on Vascular Biomaterials (ESVB), Straßbourg, 2023, oral presentation.

Kilian M. A. Mueller, Andreas Unterrainer, Diana M. Rojas-González, Marian Willner, Julia Herzen, Petra Mela, *Microporous Scaffolds for In Situ Cardiovascular Tissue Engineering via Melt Electrowriting,* 13th European Symposium on Vascular Biomaterials (ESVB), Straßbourg, 2023, oral presentation.

Salma Mansi, Zahid Hussain, Geoffrey J. Topping, Sarah Dummert, Carolin Rickert, **Kilian M. A. Mueller**, Franz Schilling, Roland Fischer, Oliver Lieleg, Petra Mela, *Antibacterial and MRI-visible Scaffolds out of Metal-Organic Framework / Polycaprolactone for Tissue Engineering Applications by Melt Electrowriting,* Tissue Engineering and Regenerative Medicine International Society (TERMIS) European Chapter Conference: Manchester, 2023, poster presentation.

Kilian M. A. Mueller, Paula Castejón Echevarne, Matthias Pixner, Petra Mela, *A Bioinspired Bizonal Mitral Valve Scaffold Via Melt Electrowriting,* Heart Valve Society Annual Meeting (HVS): Malaga, 2023, oral presentation. *Awarded with Young Investigator Best Oral Presentation Award*

Kilian M. A. Mueller, Paula Castejón Echevarne, Matthias Pixner, Petra Mela, *An Anatomically Inspired and Spatially Heterogeneous Mitral Valve Scaffold via Melt Electrowriting*, 33rd Conference of the European Society for Biomaterials (ESB): Davos, 2023, poster presentation.

Salma Mansi, **Kilian M. A. Mueller**, Geoffrey J. Topping, Zahid Hussain, Sarah Dummert, Carolin Rickert, Sebastian Schwaminger, Sonja Berensmeier, Roland Fischer, Oliver Lieleg, Franz Schilling, Petra Mela, *MRI-visible and Multifunctional Melt-electrowritten Scaffolds for Tissue Engineering Applications,* 33rd Conference of the European Society for Biomaterials (ESB): Davos, 2023, poster presentation.

Kilian M. A. Mueller, Andreas Unterrainer, Diana M. Rojas-González, Marian Willner, Julia Herzen, Petra Mela, *Tunable Microporous Scaffolds via Melt Electrowriting,* Annual Meeting of the German Society for Biomaterials (DGBM): Jena, 2023, oral presentation.

Annika Hangleiter, **Kilian M. A. Mueller**, Sarah Burkardt, Diana M. Rojas-González, Christina Kwade, Sebastian T. Pammer, Stefan Leonhardt, Petra Mela, *A Filament-based Melt Electrowriting Approach for the Fabrication of Multiscale Scaffolds,* Annual Meeting of the German Society for Biomaterials (DGBM): Jena, 2023, oral presentation.

Pietro Terranova, **Kilian M. A. Mueller**, Antonio D'Amore, Petra Mela, *Multi-axis Electro-deposition Platform to Fabricate Complex 3D Scaffolds with Controlled Micro and Macro-architecture,* Annual Meeting of the German Society for Biomaterials (DGBM): Jena, 2023, oral presentation.

Salomé Luís, Duarte Moura, **K. M. A. Mueller**, Alexander Löwen, Alicia Fernández-Colino, Jizhen Zhang, Joselito M. Razal, Petra Mela, José C. Rodríguez-Cabello, Fernão Magalhães, Helga Bergmeister, Inês C. Gonçalves, Andreia T. Pereira, *Advancing GO-Graft Towards an Implantable Anti-adhesive Vascular Graft,* XLV Congreso de la Socied Ibérica de Biomecánica y Biomateriales (SIBB): Barcelona, 2023, oral presentation.

Salomé Luís, Duarte Moura, **K. M. A. Mueller**, Alexander Löwen, Alicia Fernández-Colino, Jizhen Zhang, Joselito M. Razal, Petra Mela, José C. Rodríguez-Cabello, Fernão Magalhães, Helga Bergmeister, Inês C. Gonçalves, Andreia T. Pereira, *The GO-graft*

Odyssey: Shaping a Non-fouling Hydrogel into an Anti-adhesive Vascular Graft for Bypass Surgery, World Biomaterials Congress (WBC): Daegu, 2024, oral presentation.

Kilian M. A. Mueller, Franziska Schneider, Matthias Pixner, Paula Castejón Echevarne, Petra Mela, *A Bioinspired Fiber Composite Approach to In Situ Tissue Engineering of the Complete Mitral Valve,* Heart Valve Society Annual Meeting (HVS): Boston, 2024, oral presentation.

Pietro Terranova, **Kilian M. A. Mueller**, Antonio Pantano, Antonio D'Amore, Petra Mela, *5-Axes Melt Electrowriting Platform to Fabricate 3D Bioinspired Fibrous Heart Valve Scaffolds with Controlled Micro and Macro-Architecture,* Heart Valve Society Annual Meeting (HVS): Boston, 2024, oral presentation.

Kilian M. A. Mueller, Matthias Pixner, Franziska Schneider, Paula Castejón Echavarne, Petra Mela, *A Bioinspired Microfiber-based Mitral Valve Scaffold via Melt Electrowriting,* 11th Cardiovascular Research Days: Weissensee, 2024, poster presentation.

Yuan-Tsan Tseng, **Kilian M. A. Mueller**, Sanida Vaz, Rudolf Hellmuth, Najma Latif, Petra Mela, Magdi Yacoub, *Novel Multiscale Tissue Engineered Scaffold for Heart Valve Tissue Engineering*, BioMedEng24: London, 2024, oral poster.

Kilian M. A. Mueller, Matthias Pixner, Franziska Schneider, Paula Castejón Echavarne, Petra Mela, *Engineering Biomimetic Mitral Valve Scaffolds: A Hybrid Approach for In Situ Tissue Engineering*, 8th China-Europe Symposium on Biomaterials in Regenerative Medicine (CESB): Nuremberg, 2024, oral presentation.

Kilian M. A. Mueller, Christina Ahrens, Linda Grefen, Felix Kur, Christian Hagl, Petra Mela, *Small-diameter Vascular Grafts with Tunable Compliance via Melt Electrowriting*, 19th Biennial Meeting of the International Society for Applied Cardiovascular Biology (ISACB): Vienna, 2024, poster presentation.

Salomé Luís, Duarte Moura, **Kilian M. A. Mueller**, Alexander Löwen, Alicia Fernández-Colino, Jizhen Zhang, Joselito Razal, Petra Mela, José Rodríguez-Cabello, Cristina Barrias, Fernão Magalhães, Helga Bergmeister, Inês Gonçalves, Andreia Pereira, *GO-Graft: From Hydrogel to Anti-Adhesive Vascular Graft for Bypass Surgery,* 19th Biennial Meeting of the International Society for Applied Cardiovascular Biology (ISACB): Vienna, 2024, poster presentation.

Kilian M. A. Mueller, Matthias Pixner, Michael Pressnig, Franziska Schneider, Paula Castejón Echavarne, Petra Mela, *Hybrid Engineering of Biomimetic Mitral Valve*

Scaffolds for in situ Tissue Engineering, Annual Meeting of the German Society for Biomaterials (DGBM): Berlin, 2024, poster presentation.

Kilian M. A. Mueller, Matthias Pixner, Michael Pressnig, Franziska Schneider, Paula Castejón Echavarne, Petra Mela, *Hybrid Biofabrication of an Anatomically and Mechanically Accurate Mitral Valve Scaffold for in situ Tissue Engineering via Multiscale Fiber Deposition,* International Conference on Biofabrication: Fukuoka, 2024, oral presentation.

Pietro Terranova*, **Kilian M. A. Mueller***, Dominic Biebl, Antonio Pantano, Antonio D'Amore, Petra Mela, *5-Axes Melt Electrowriting Platform to Fabricate 3D Bioinspired Fibrous Heart Valve Scaffolds with Controlled Micro and Macro-Architecture,* International Conference on Biofabrication: Fukuoka, 2024, poster presentation. * equal contribution

Patent Applications

WO 2022/117667 A1: *Electro-spinning/Writing System and Corresponding Method,* **Kilian M. A. Mueller**, Sarah Burkhardt, Stefan Leonhardt, Sebastian Pammer, Petra Mela, Johannes Schweiger, disclosed.

WO 2022/122734 A1: *Melt Electro-writing System and Corresponding Method,* **Kilian M. A. Mueller**, Sarah Burkhardt, Petra Mela, Stefan Leonhardt, Sebastian Pammer, Johannes Schweiger, disclosed.

WO 2023/006989 A1: *Method and Device for Producing a Coated Object by Means of Additive Manufacturing in a Vacuum,* **Kilian M. A. Mueller**, Petra Mela, Markus Eblenkamp, Nicolas Niessen, disclosed.

Some of the first author publications have been used in this work. The permission for reuse was obtained from the respective copyright owners.

Dank

Mein tiefer Dank gilt den Unterstützern dieser Arbeit.

Edel sei der Mensch,
Hülfreich und gut!
Denn das allein
Unterscheidet ihn
Von allen Wesen,
Die wir kennen.

Johann Wolfgang von Goethe, Das Göttliche, 1. Strophe

Appendix